NASA/TP–20220007254

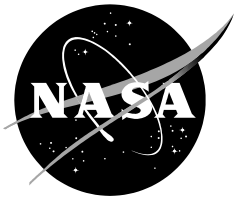

Global Energy and Water Exchanges Program Surface Radiaton Budget Release 4 Integrated Product

Algorithm Theoretical Basis Document

Paul W. Stackhouse, Jr.

Langley Research Center, Hampton, Virginia

Stephen J. Cox, J. Colleen Mikovitz and Taiping Zhang
Science Systems and Applications, Inc., Hampton, Virginia

May 2022

NASA STI Program Report Series

The NASA STI Program collects, organizes, provides for archiving, and disseminates NASA's STI. The NASA STI program provides access to the NTRS Registered and its public interface, the NASA Technical Reports Server, thus providing one of the largest collections of aeronautical and space science STI in the world. Results are published in both non-NASA channels and by NASA in the NASA STI Report Series, which includes the following report types:

- TECHNICAL PUBLICATION. Reports of completed research or a major significant phase of research that present the results of NASA Programs and include extensive data or theoretical analysis. Includes compilations of significant scientific and technical data and information deemed to be of continuing reference value. NASA counterpart of peer-reviewed formal professional papers but has less stringent limitations on manuscript length and extent of graphic presentations.

- TECHNICAL MEMORANDUM. Scientific and technical findings that are preliminary or of specialized interest, e.g., quick release reports, working papers, and bibliographies that contain minimal annotation. Does not contain extensive analysis.

- CONTRACTOR REPORT. Scientific and technical findings by NASA-sponsored contractors and grantees.

- CONFERENCE PUBLICATION. Collected papers from scientific and technical conferences, symposia, seminars, or other meetings sponsored or co-sponsored by NASA.

- SPECIAL PUBLICATION. Scientific, technical, or historical information from NASA programs, projects, and missions, often concerned with subjects having substantial public interest.

- TECHNICAL TRANSLATION. English-language translations of foreign scientific and technical material pertinent to NASA's mission.

Specialized services also include organizing and publishing research results, distributing specialized research announcements and feeds, providing information desk and personal search support, and enabling data exchange services.

For more information about the NASA STI program, see the following:

- Access the NASA STI program home page at http://www.sti.nasa.gov

- Help desk contact information:

https://www.sti.nasa.gov/sti-contact-form/ and select the "General" help request type.

NASA/TP–20220007254

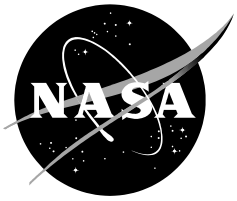

Global Energy and Water Exchanges Program Surface Radiation Budget Release 4 Integrated Product:

Algorithm Theoretical Basis Document

Paul W. Stackhouse, Jr.

Langley Research Center, Hampton, Virginia

Stephen J. Cox, J. Colleen Mikovitz and Taiping Zhang
Science Systems and Applications, Inc., Hampton, Virginia

National Aeronautics and
Space Administration

Langley Research Center
Hampton, VA 23681

May 2022

Acknowledgments

We acknowledge the long-term contributions of the SRB project by Dr. Shashi Gupta, who is now retired. This work was supported by NASA's Science Mission Directorate under Dr. Jack Kaye (WBS 509496.02.80.01.09) and Radiation Sciences Program administered by Dr. Hal Marring (WBS 281945.02.80.01.42).

Abstract

This document represents the Algorithm Theoretical Basis Document (ATBD) describing the NASA Langley Research Center's Surface Radiation budget (SRB) developed in collaboration with the World Research Climate Programme's Global Energy and Water Exchanges Program. The top of atmosphere and surface fluxes span from July 1, 1983 through June 30, 2017. The shortwave or solar wavelengths span the entire record. The thermal infrared or longwave fluxes span globally from January 1, 1988 to December 30, 2009. Before 1988, only the land-only fluxes are available. After 2009 only the ocean fluxes are available. This document describes all the inputs and radiative transfer algorithms used to generate the TOA and surface radiative fluxes. The fluxes include upward and downward, all-sky, clear-sky and pristine sky conditions. Surface net fluxes and cloud radiative effect are computed and presented as part of the analysis. Comparisons to other data products are made to assess the top-of-atmosphere and surface fluxes. Additionally, surface measurements are utilized to validation the surface fluxes. The surface validation analysis shows the the radiative fluxes are improved compared to the previous version. Data set cautions are also presented.

This report is available in electronic form at

https://gewex-srb.larc.nasa.gov

1 Introduction to the GEWEX SRB Rel. 4 Integrated Product Data Set

The World Climate Research Programme (WCRP) organized and initiated the creation of multiple projects to build and assess measures of cloud and radiative processes of the Earth-atmosphere system in the 1980's (Suttles and Ohring, 1986). Projects estimating global cloud, atmospheric temperature and water vapor, precipitation and radiation were established. One of those projects was the Surface Radiation Budget project (SRB). Later as WCRP organized into the Global Energy and Water-cycle Experiment (and now Exchanges program called GEWEX), these data sets had derived long-term products providing information about global variability of energy and water cycles. SRB's first data set was released in 1992 (Whitlock et al, 1995), with a second version in 2000. Release 3 was issued in 2010 (Stackhouse et al, 2011). Since then, GEWEX reorganized to formulate the Data and Assessments Panel (GDAP) aimed at performing community assessments of the long-term global data products with focus on integrating various data products to address issues in the closing of the global energy and water cycles (Kummerow et al. 2019). This SRB Release 4 data set integrates data products from the cloud, aerosol, atmosphere, ocean surface, and land surface projects, coordinating within GDAP to produce a long-term time series of TOA and surface radiative estimates. Figure 1 shows the time span for the new SRB SW (shortwave or solar irradiances) and LW (longwave or thermal infrared irradiances) data products together with key inputs and validation data products.

This document describes the various inputs, algorithm changes, and data products produced in this new version. The data products are compared to both surface and satellite-based estimates from other radiative data products. The long-term averages and variability are described and compared to other data products. Known issues with input and output data products are described in section 7.4 for user reference.

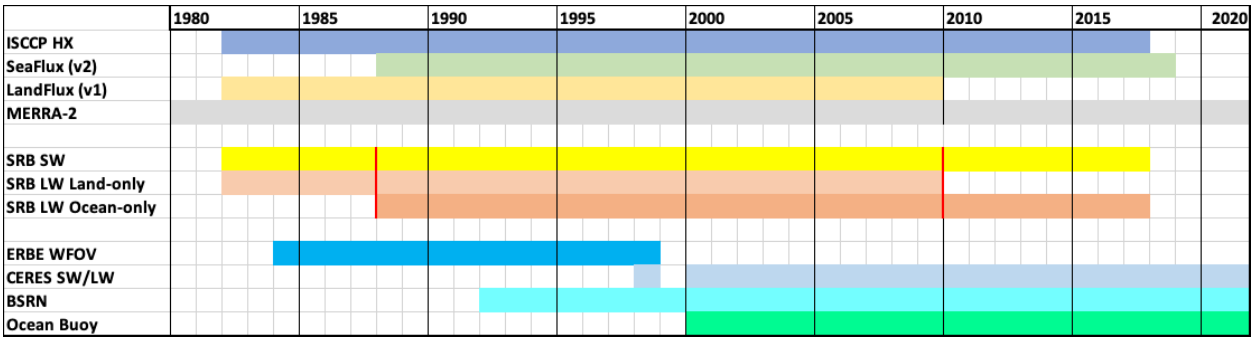

Figure 1. Time spans of GEWEX SRB Release 4 Integrated Product (R4-IP), key inputs and comparison data products.

2 ISCCP HXS Summary of Changes and Updates

ISCCP reprocessed and released its entire dataset, replacing the D series (Rossow et al. 1996) with the H series (Young et al. 2018). SRB uses the pixel level products from ISCCP, called DX in the D series and now HXS in the H series. The product is based on two channels shared across instruments and platforms: a visible channel centered on 0.65 μm, and an infrared channel centered on 10.5 μm. A schematic of the new processing flow is shown and summarized in Figure 2.

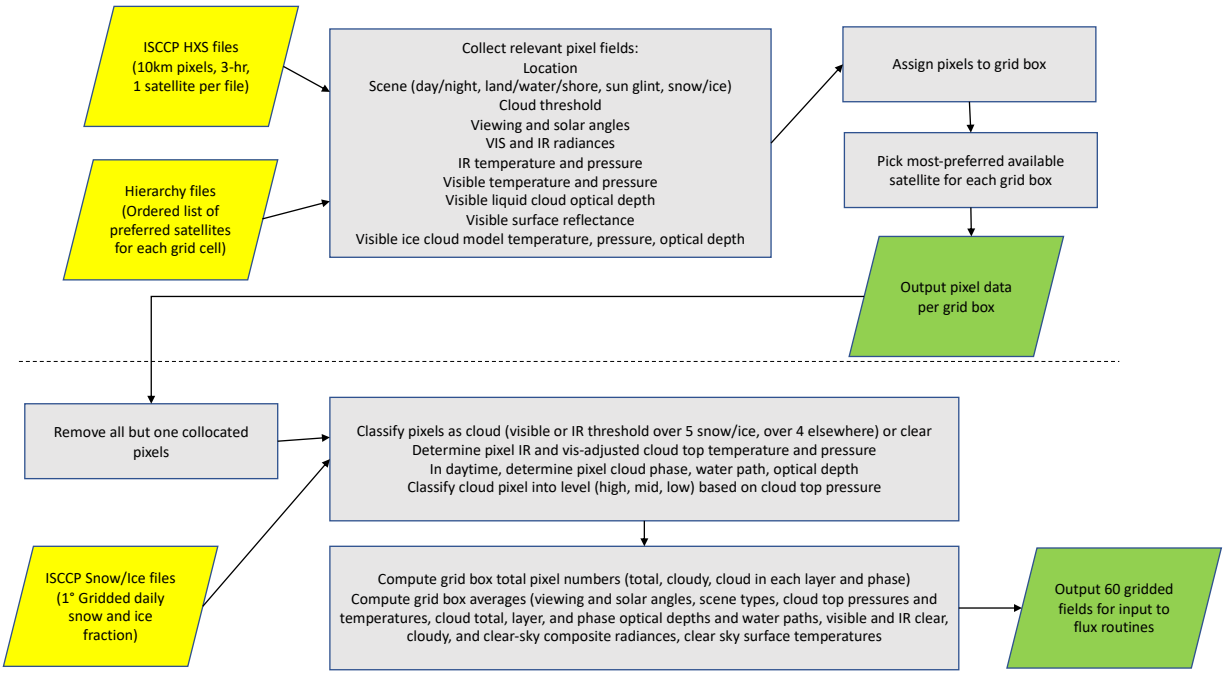

Figure 2. Flow diagram for processing of ISCCP HXS and Snow/Ice files for use in SRB flux algorithms.

2.1 Calibration

All radiances are normalized to a reference afternoon polar orbiter. As briefly described in Young et al. (2018), from the beginning of the data set through 2009, the absolute reference is the AVHRR aboard NOAA-9. After 2009, the absolute reference in the HXS product switches to NOAA-18. These differences in calibration procedure represent an update to the more detailed description provided in Rossow et al. (1996), section 6.2.2. Note that the uncertainties of the IR channel calibration and the visible channel are specified as +/- 1 K and +/- 3% respectively. Other innovations relative to ISCCP D-series include that the geostationary normalization process has now been fully automated and uses all radiance data whereas DX used only a small sample.

2.2 Pixel density increase

The DX product was based on the B3 dataset, which was subsampled to 30 km horizontal and 3-hourly temporal resolution. HXS uses the B1U (geostationary) and GAC (AVHRR) data, at 10 km and 3-hourly resolutions. The pixel level product equivalent to the DX product is now called HXS. The higher resolution allows an approximately ninefold increase in the number of pixels per grid box compared with SRB Release 3 (Rel3). Currently, SRB uses a nested grid which is 1°x1° from 45°S to 45°N, transitioning to 1°x120° at the poles (see Appendix B for a complete description). The SRB Release 4-Integrated Product (Rel4-IP) therefore allows up to ~81 pixels per grid box, up from ~9 for Rel3. Due to the increased number of pixels, the cloud fraction is now able to take on a much greater number of values and other cloud and surface properties are statistically more robust.

2.3 NIR channel no longer used

The DX used the 3.7 μm near-IR channel on AVHRR as an additional input into cloud detection over polar regions. Because NOAA began a day/night switch between this channel and the 1.6 μm channel, HXS has removed the NIR channel for cloud detection, with the general result of detecting fewer clouds over ice.

2.4 New water/ice optical property models

In the HXS radiance model, liquid cloud droplet effective radius has been changed from 10 μm everywhere to 13 μm over land and 15 μm over ocean. Ice particle effective radius has changed from 30 μm everywhere to 20 μm for thin clouds with optical depths less than 3.55, and 34 μm for thicker clouds.

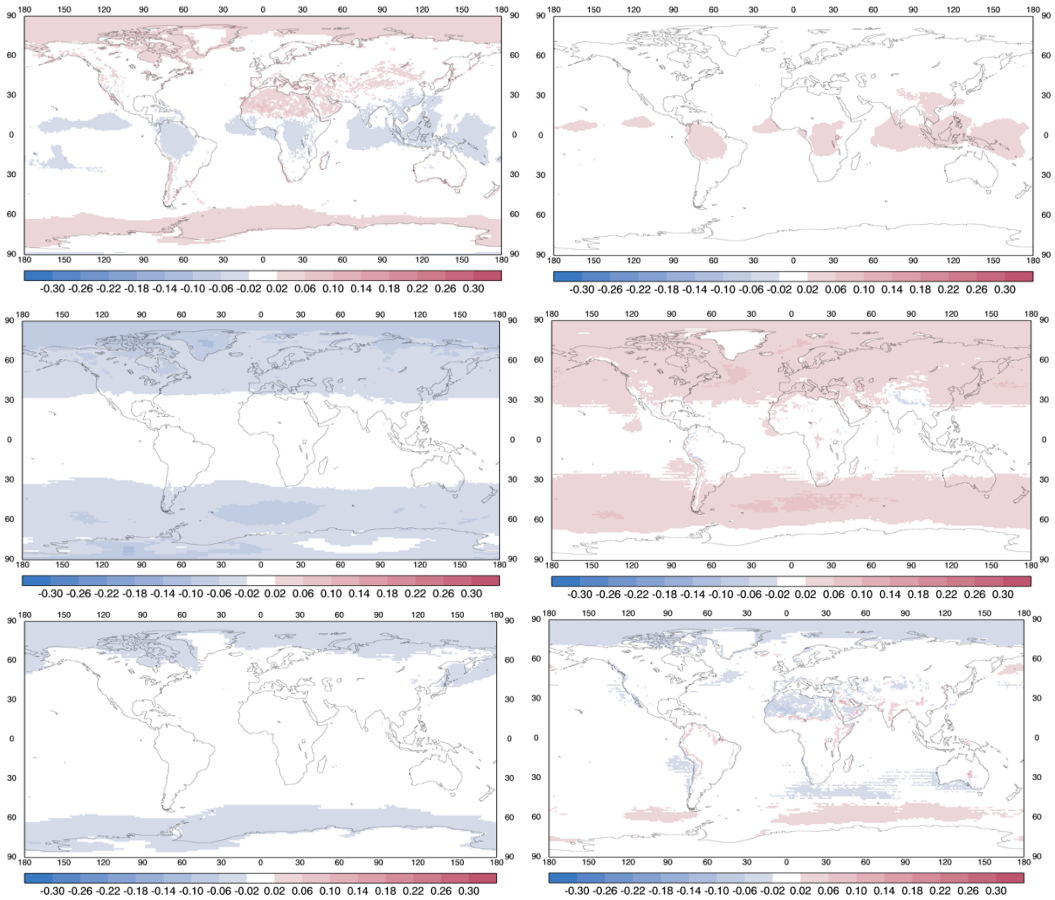

Figure 3. Long-term average changes in cloud amount from SRB processed ISCCP D series to H series. From top: High Ice, High Liquid (category did not exist in D series), Mid Ice, Mid Liquid, Low Ice, Low Liquid.

2.5 Ice/Water cloud temperature threshold moved to 253K

Ice clouds are now assumed for cloud top temperatures 253K and below; this is a substantial reduction from the DX value of 260K. The liquid/ice partitioning is thus shifted towards liquid clouds in the intermediate temperature range, leading to an increase in the liquid cloud fraction relative to ice clouds. Figure 3 shows the differences in long term cloud fraction

from DX to HXS for ice vs liquid clouds, and at the three ISCCP height ranges defined by the cloud top pressure (pc). The cloud layers are designated as high (pc < 440 hPa), middle (440 ≤ pc ≤ 680 hPa) and low (pc > 680 hPa) layers. The primary impact of the reduction in the ice vs. water threshold temperature appears in the middle height range in the midlatitudes and polar regions. Note that the cloud phase is only determined during daytime. There are day/night differences in cloud fraction, therefore the DX to HXS changes in liquid and ice cloud fractions do not necessarily add up to the overall cloud fraction changes, nor the overall layer cloud fraction changes.

2.6 High water cloud added

ISCCP DX did not allow for high liquid clouds. HXS adds that category due to the reduction of the cloud top temperature threshold noted above. High liquid cloud amount is now around 0.7% globally.

3 SRB ISCCP Data Processing Changes

3.1 Reassessment of assumptions regarding CTT averaging

Grid box averaging of cloud top temperature (CTT) has been changed to better match ISCCP practices. Previously each pixel's temperature had been converted from count to temperature through a conversion table and then the temperatures averaged to produce a grid box temperature. It is more accurate to instead average the counts first, then convert to a cloud top temperature. In addition, an infrequent (0.3%) ambiguous occurrence has been addressed. ISCCP provides cloud top temperatures computed for an ice cloud and for a liquid cloud. On rare occasions, the ice cloud model produces a CTT greater than 253K and the liquid cloud model produces a CTT less than 253K, leaving the phase of the cloud ambiguous. In these cases, the colder liquid cloud model temperature is used, and the phase is reported as ice.

3.2 Change in cloud thresholding over snow and ice surfaces

The detection of clouds over snow and ice surfaces has traditionally been a difficult remote sensing problem. ISCCP HXS produced considerably higher cloud fractions over snow and ice than DX did. SRB has addressed this by changing the cloud thresholding requirements. As before, a pixel over non-snow/ice surfaces continues to be declared a cloud if either the IR threshold or visible threshold reported is 4 or 5. We now require an IR or VIS threshold of 5 over snow and ice for a cloud to be declared. This reduces the cloud fractions over the Arctic and Antarctic back to levels more in agreement with other data sets. For the H series, ISCCP uses MAC v1 (Kinne et al., 2013) aerosols in its retrievals, the result of which is the detection of more clouds over high aerosol land areas, especially in Africa and south Asia. Concurrently, the elimination of the 3.7 μm channel in the H series reduced cloud detection over polar areas. The increased threshold requirements for cloud over ice in the SRB processing further reduces cloud amounts over polar areas.

3.3 Removal of duplicate pixels

ISCCP HXS provides navigation of individual satellite pixels to a resolution of 0.1° latitude and 0.1° longitude. With the increased number of pixels available in the HXS dataset, this results in numerous instances of different pixels from the same satellite having the same location. During the processing of HXS data for SRB use, only the first instance of a pixel at a given location is retained for use.

3.4 Cloud Filling assumption changes

For this release, a new algorithm was developed to fill in gaps in the cloud property data, as used by the longwave algorithm (see Figure 4). Gaps are present in the data if there are no satellite data, or the area is within a sun glint region. The cloud filling is performed on the output of the initial gridding and averaging of the pixel values, shown as the last box on the flow diagram in Figure 3. While assumptions from the previous version are similar, there are some changes. Temporal interpolation now includes the last hour of the previous day and the first hour of the next day, even across month or year boundaries. Rel3 procedure was to only use the previous day if there were no valid values in the day of interest. Most filling is accomplished by temporal averaging. Logarithmic averaging is used for optical depth, linear averaging for all other fields, such as cloud top temperature. After the initial averaging, adjustments to filled cloud top temperatures and optical depths are made to match filled cloud amounts. If any cloud property is filled within a grid box, a flag value is assigned. A flag value of 2 indicates surrounding hours were present for temporal averaging, a flag equal to 1 indicates only one adjoining hour (replication). Flag values are included within the data files of the longwave

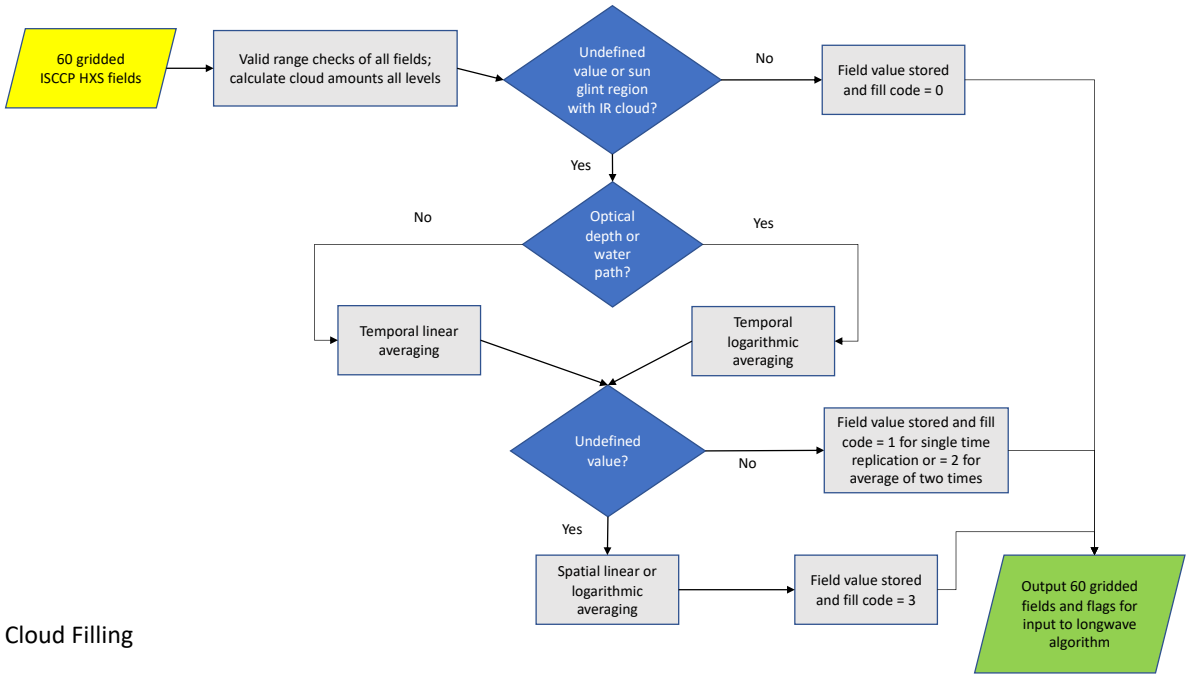

Figure 4. Flow diagram for filling gaps in ISCCP data, prior to processing in SRB longwave algorithm fluxes.

A summary of the general procedure for Rel4-IP is as follows and illustrated in Figure 4.

1. Check all values for validity.
2. Calculate cloud amounts from pixel counts.
3. Fill regions where no satellite data was present.
4. Fill sun glint regions if there is a valid IR cloud indicated.
5. Any remaining grid box that should have a cloud or surface property is filled by averaging surrounding grid boxes (spatially). A flag value of 3 is assigned for spatial averaging.

3.5 Overall cloud changes

The combination of changes in ISCCP processing and changes in SRB processing of ISCCP data has led to changes in cloud properties. Figure 5 shows the overall differences in cloud amount. ISCCP's processing changes result in a reduction in cloud amount over Greenland and Antarctica, and an increase over tropical and midlatitude land, especially over Africa and southern Asia. SRB changes, primarily the requiring of a stricter cloud threshold over snow and ice, have led to a ~2% reduction in global cloud cover.

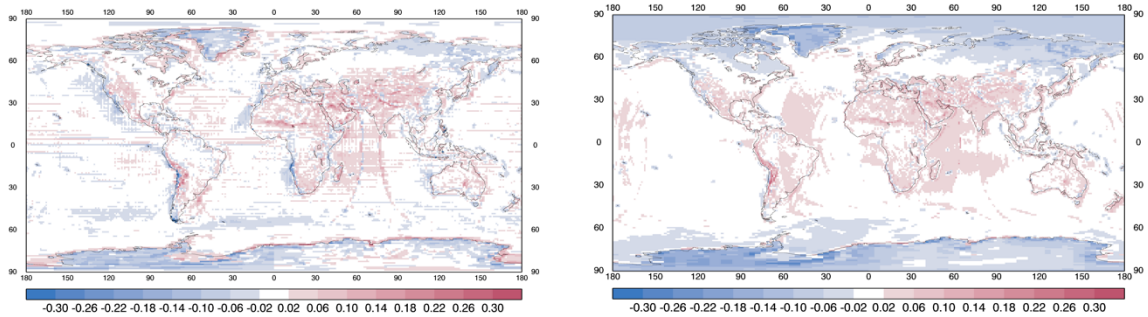

Figure 5. Long-term average changes in cloud fraction. Left: differences between HGM (ISCCP monthly average H series) and D2 (ISCCP monthly average D series). Right: differences between SRB processed ISCCP HXS (Rel4) and SRB processed ISCCP DX (Rel3).

The addition of high liquid clouds in the ISCCP H series, and the reduction of the cloud top temperature threshold for ice vs liquid clouds to 253K has shifted clouds from liquid to ice, as shown in Figures 3 and 5 according to the various cloud levels defined in Section 2. (Please note that the cloud top pressure assignment depends upon the temperature structure of the atmosphere which is also new in the H series, see Section 4.2). Histograms of cloud fraction (Figure 6) indicate that the increased number of HXS pixels in a grid cell allows the representation of a more continuous variation in cloud fraction than was allowed by DX. More specifically, the cloud amount histograms show a reduced middle and low ice amounts with the latter decreasing to near zero.

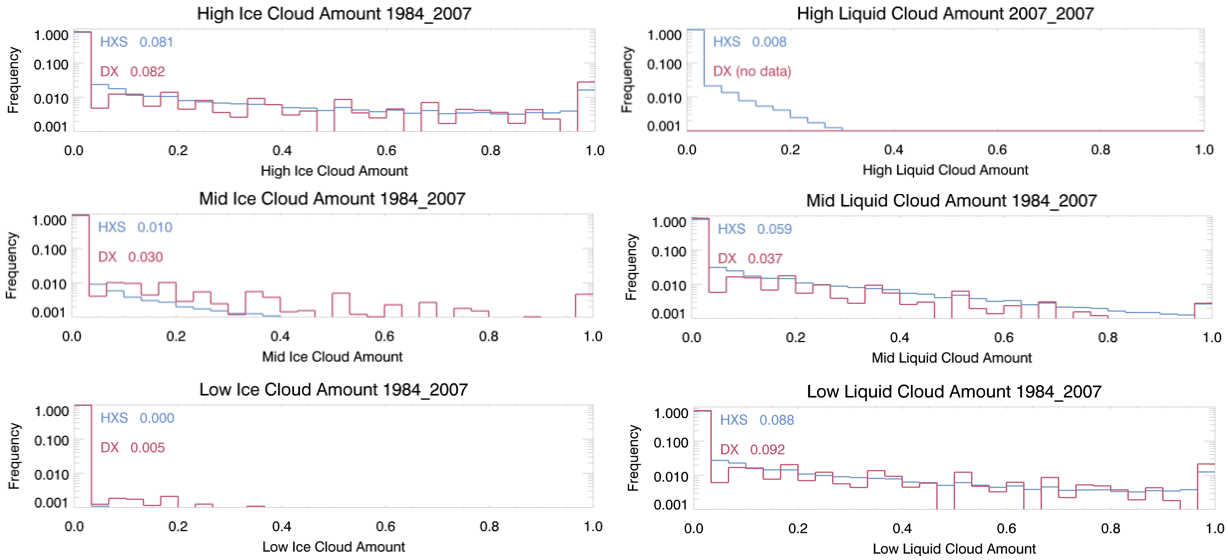

Figure 6. SRB processed changes in cloud amount from ISCCP D series to ISCCP H series, by cloud phase and cloud height.

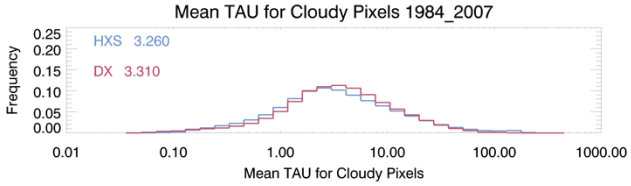

Figure 7. Long term histogram of cloud optical depth from SRB-processed ISCCP DX series to SRB-processed HXS series.

There is little overall change in ISCCP-derived cloud optical depth from DX to HXS (Figure 7) however there is substantial change in the distribution of optical depth by phase and height (Figure 8). The shift from ice to liquid has left the remaining ice clouds substantially thicker for middle and low cloud layers but slightly thinner for high cloud ice on average. The mean optical depth distributions for middle and low water clouds are only slightly thinner.

4 General Input Changes

4.1 Aerosol changed from climatology to MAC v1

Aerosol in Rel3 contained only a fixed maritime and a fixed continental aerosol. Rel4-IP now includes a fully variable composition aerosol, using the Max-Planck Aerosol Climatology (MAC, Kinne et al., 2013).

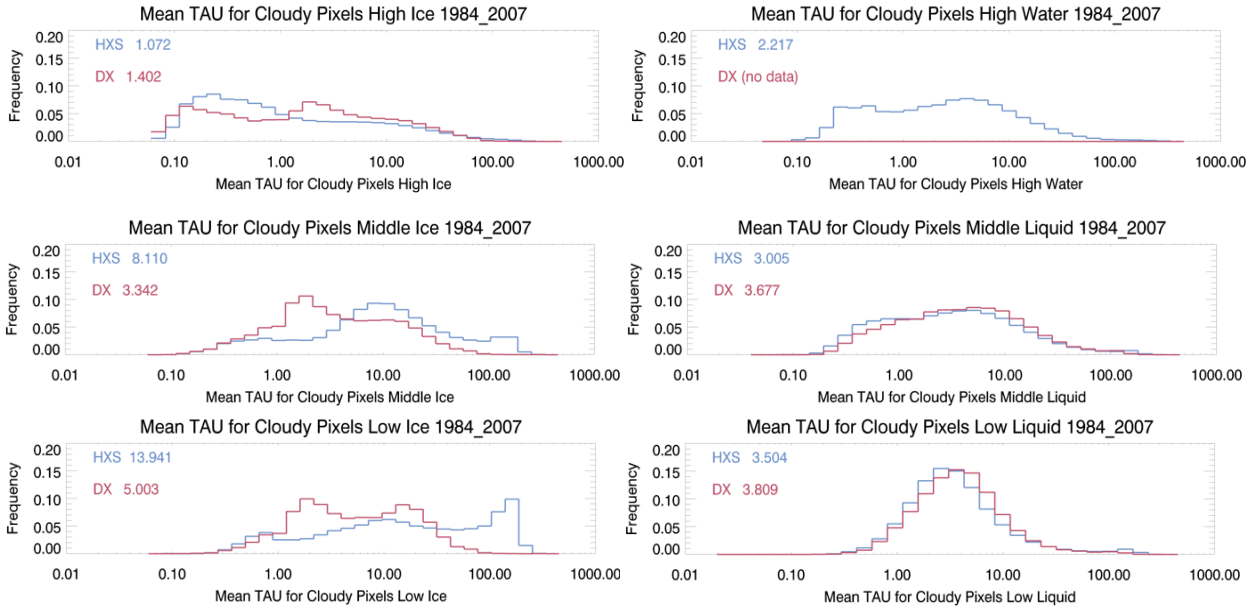

Figure 8. Long-term histogram of cloud optical depth from SRB-processed ISCCP DX series to SRB-processed HXS series, separated by cloud height and content.

4.1.1 Description of old aerosol optical properties

Rel3 contained aerosols with fixed single scatter albedo and asymmetry parameter, varying only by continental or maritime surface type. Maritime aerosols were less absorptive and more forward scattering than continental aerosols. The amount (optical depth) of aerosols was variable. An initial climatological value was used to fix surface albedo. The absolute value was then allowed to vary to produce a value of TOA flux which matches that observed by the satellite. Rel3 chose the initial value based on a monthly modal optical depth from MATCH (Collins et al. 2001). The mode was chosen instead of monthly average to provide a background value. As high aerosol events are episodic, the mode is lower than the monthly average.

4.1.2 Description of MAC v1 optical properties

Aerosol now includes asymmetry parameter and single scattering albedo as inputs, with the MACv1 dataset providing monthly values of each, allowing a continuous range of aerosol composition (homogenous mixture assumed). The initial value of optical depth is also taken from MACv1, though reduced by 20% to provide a background value. To avoid step changes from month to month, an implied daily value of all optical properties is used (Zhang et al. 2017). The daily values are chosen to vary smoothly while preserving the correct monthly average.

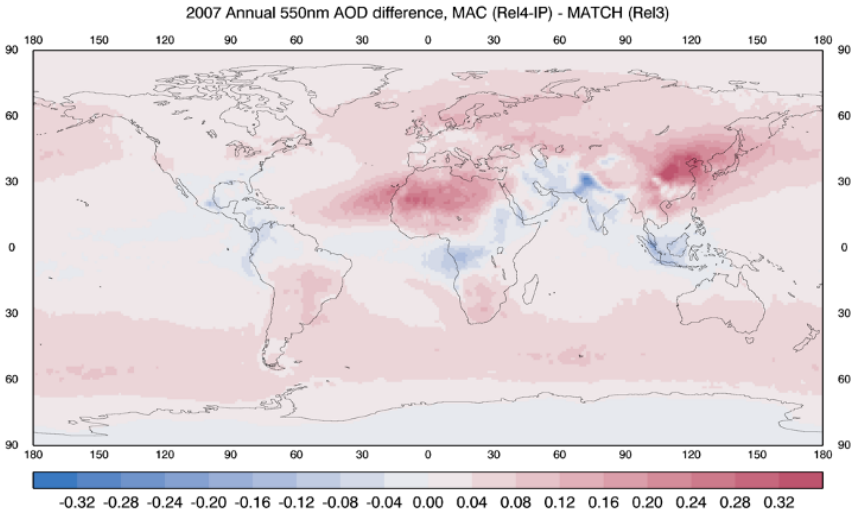

Figure 9. Difference in annual mean input optical depth for year 2007 between Rel4 (MAC) and Rel3 (modal MATCH).

4.1.3 Contrast between old and new aerosol

Figure 9 shows the difference in mean input aerosol optical depth. Aerosol increases in the desert dust Saharan and Tibetan regions, and the southern hemisphere midlatitude ocean. It is reduced over the Indian subcontinent and marine continent, and over Antarctica.

4.2 ISCCP NNHIRS temperature and water vapor data set

Atmosphere and surface meteorology (temperature and water vapor) for this release mainly originates from the ISCCP NNHIRS dataset (Rossow 2017). It is part of the Ancillary Data Products available by request from NCEI (https://www.ncdc.noaa.gov/cdr/atmospheric/cloud-properties-isccp). The dataset adapts the HIRS neural net retrieval by Shi et al. (2016) by adding levels to the upper atmosphere, clearing cloud-contaminated values, and filling in missing

data. Because meteorology is key for the calculation of longwave fluxes, the limitations and differences with NNHIRS and other data sets are explored in the subsections here.

4.2.1 Limitation: large amount of filled data

As explained in the ISCCP ATBD (Rossow 2017) the HIRS data providing the basis for the NNHIRS data set covers 30% of the earth surface every six hours if there are two operational satellites. For global 3-hourly coverage, this translates to a large amount of filled data Figure 10 shows that daily over land, there are about 10% instantaneous retrieved satellite values at any given time. 30-40% of the values are filled with data from within one observation day. However, there are stretches of time when that metric drops to 5%, with the bulk of the filling coming from the 30-day principal component analysis (PCA). This can show up in the flux anomalies for clear-sky downwelling longwave flux (DLF, black line in Figure 10, right axis), for example as seen in mid-1995. Over oceans, most of the values are from a 5-day linear average with only 5% instantaneous data.

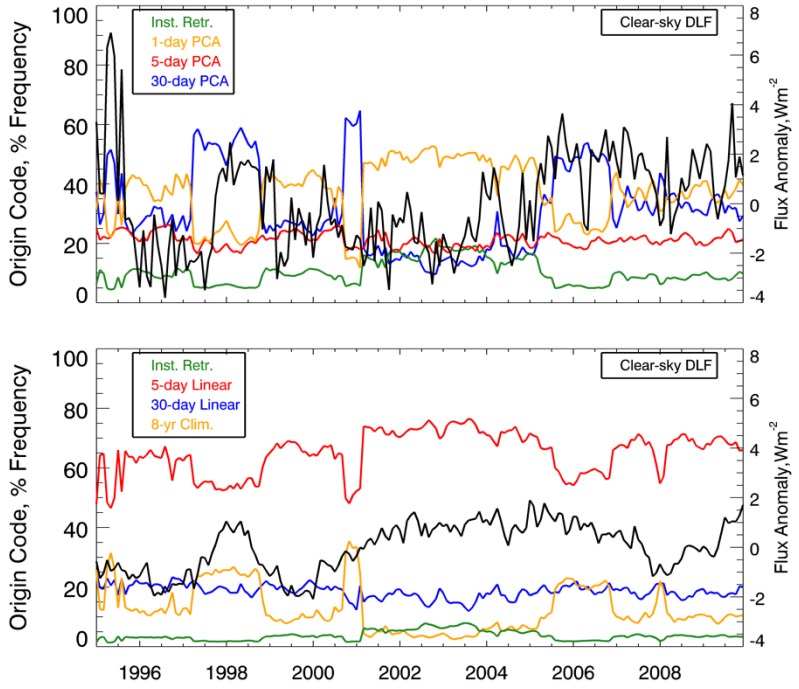

Figure 10. Figure 10. Top: Monthly average of daily histograms of the land-only grid box origin codes for the NNHIRS data compared with flux anomaly of clear-sky DLF. Green is percent per day of original values; gold, red, and blue are 1-, 5-, and 30-day day principal component analysis filling, respectively. Bottom: Same as left, but for ocean-only grid boxes. Green are original values; red and blue are 5- and 30-day linear average filling, while gold is the 8-year climatology.

4.2.2 Differences relative to other data sets

Assessing NNHIRS profile temperature against MERRA-2 and the Remote Sensing Systems (RSS) temperature lower stratosphere (TLS) and temperature lower troposphere (TLT) (Mears and Wentz 2017, 2009) shows a possible problem with NNHIRS in the lower stratosphere before 1985 (Figure 11). Here both the NNHIRS and the MERRA-2 are integrated over the effective

depth of the RSS retrievals (3-8 km for TLT and 8+ km for TLS). The response after the 1991 Mt. Pinatubo eruption recovers more quickly than either MERRA-2 or RSS (although it is not clear how independent these data products are since MERRA-2 assimilates the channels from which RSS derives their product). In the TLT, the issue of larger positive anomalies in the earlier years is present but not at the amplitude of the TLS, however the larger positive anomalies begin 1991 and before. Interestingly, the Mt. Pinatubo reaction in the TLT is present in NNHIRS, but not as much in RSS or MERRA-2. Otherwise, the anomaly time series appear to be similar for both layers.

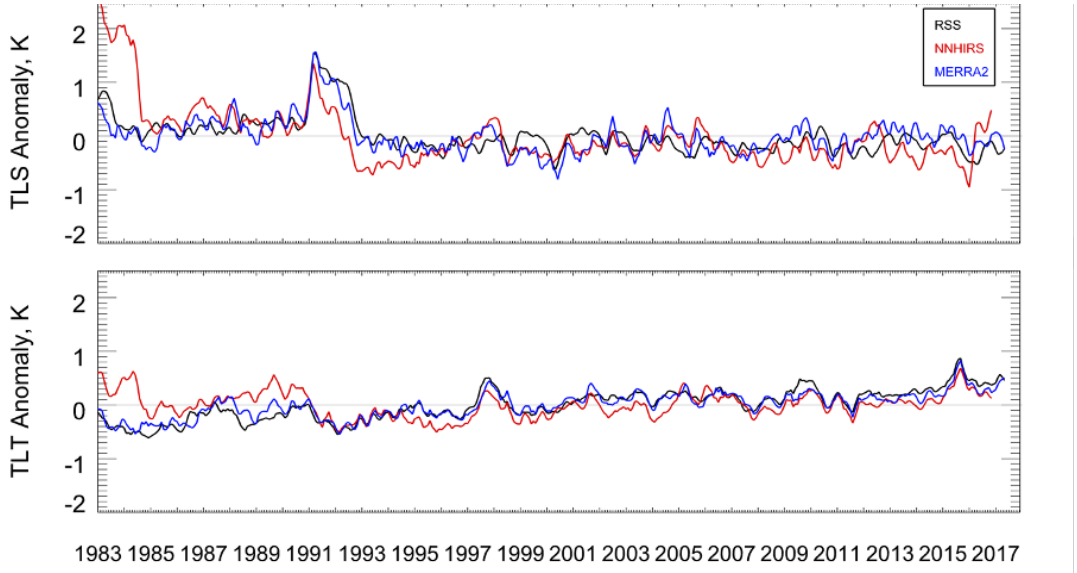

Figure 11. Three-month running means of monthly anomalies for Jul. 1983 through Dec. 2017. Top panel is the temperature in the lower stratosphere for RSS (black), NNHIRS (red) and MERRA-2 (blue). The bottom panel is temperature in the lower troposphere.

The land-only and ocean-only absolute differences between NNHIRS and MERRA-2 (GMAO, 2017d) for profile temperature are shown in Figure 12. NNHIRS is generally warmer than MERRA-2 above 200 hPa but colder below. For land-only grid boxes, the colder NNHIRS continues to the surface, but over the oceans it becomes warmer than MERRA-2. In test runs of the longwave algorithm using only NNHIRS, these warmer values were apparent in validations against buoys and in comparisons to other flux data sets. Because of this, the decision was made to use MERRA-2 over the oceans for the lower levels in the longwave algorithm (further described in section 5.4) for Rel4-IP.

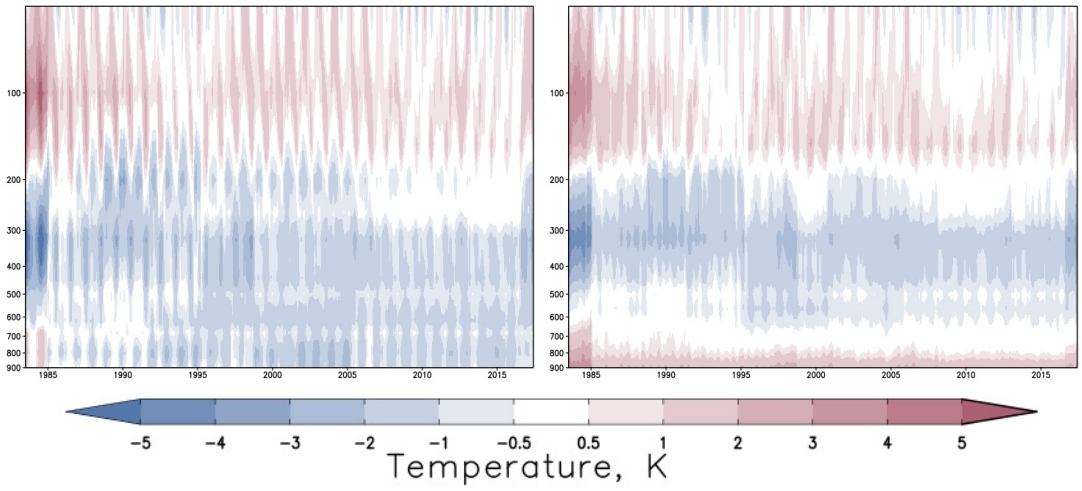

Figure 12. Profile temperature time vs. height cross-section of the absolute difference between NNHIRS and MERRA-2 for land-only (left) and ocean-only (right) averages.

Atmospheric water vapor from NNHIRS shows significant differences in both anomalies and absolute values. Seen in Figure 13, NNHIRS has a large positive bias in specific humidity at the beginning of the time series near the ocean surface compared to MERRA-2. Since most of the water vapor in the total column is near the surface, this is also seen in the total precipitable water (***Figure 14***). While at times the anomalies from NNHIRS correlate at times with MERRA-2 and RSS, there are many instances of NNHIRS missing the peaks and valleys of the timeseries. In an absolute sense, other than the near-surface ocean, the specific humidity from NNHIRS is lower than MERRA-2. The GEWEX water vapor assessment (Schröder et al. 2019, 2018) confirms many of the findings here, including the downward trend in NNHIRS seen in ***Figure 14***.

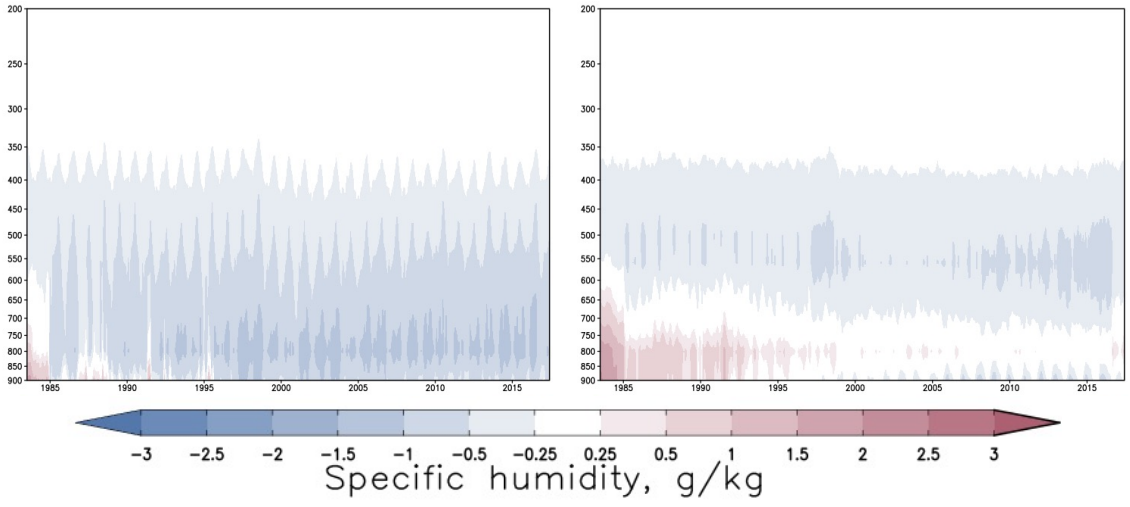

Figure 13. Profile specific humidity time vs. height cross-section of the absolute difference between NNHIRS and MERRA-2 for land-only (left) and ocean-only (right) averages.

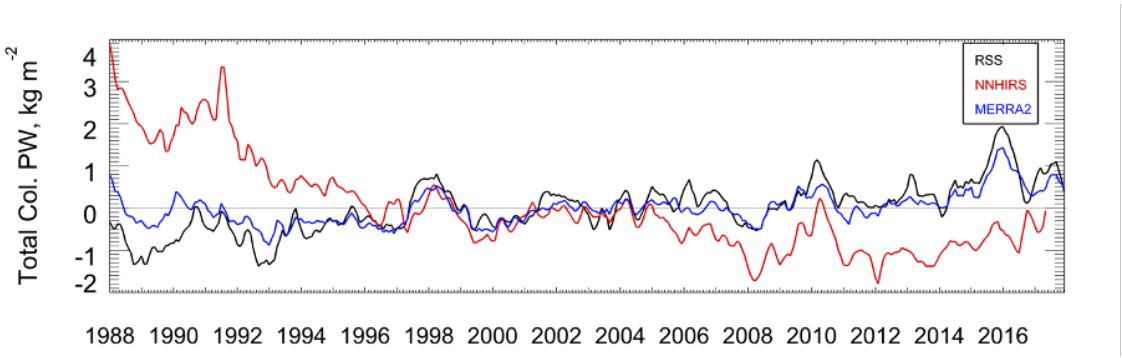

Figure 14. Three-month running means of monthly anomalies of total column precipitable water, in kg m-2, for Jan. 1988 through Dec. 2017 for ocean-only within latitude range 55ºS to 55ºN. Shown are RSS (black, average for period=30.6 kg m-2), NNHIRS (red, 30.8) and MERRA-2 (blue, 30.6).

The Rel3 version of the fluxes used the GMAO's GEOS-4 reanalysis (Suarez et al. 2005) for input meteorology. Many of the patterns present in the difference between MERRA-2 and NNHIRS are also present for the difference between NNHIRS and GEOS-4. Figure 15 gives a general sense of the patterns of water vapor (through the total column precipitable water, left) and the surface temperature (right). The increased amount of water vapor in the subsidence regions of the ocean of NNHIRS was one of the reasons which led to the use of MERRA-2 in the longwave algorithm in the lower part of the atmosphere over the oceans.

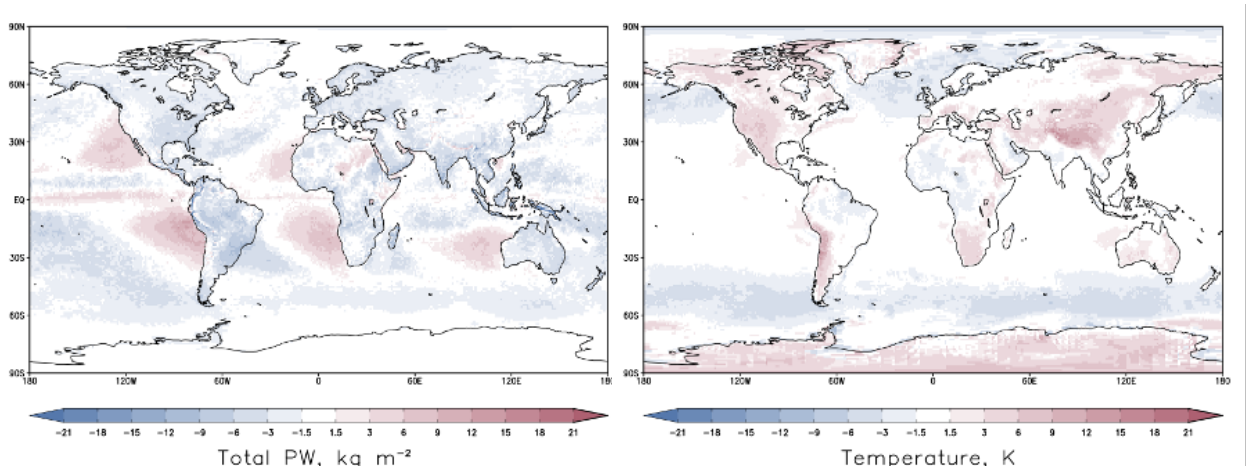

Figure 15. The 2007 annual average difference between NNHIRS and GEOS-4 total column water vapor (kg m-2), left, and 2 m temperature (K, right).

5 Longwave Algorithm Changes

The SRB longwave product issued as Rel3.1 in 2011 covered the period from July 1983 through December 2007 (Stackhouse et al., 2011). The core of the algorithm for Rel3.1 was based on the methodology described in Fu and Liou (1992). Cloud and radiance properties were based on the ISCCP DX dataset (Rossow et al., 1996). Total atmospheric water vapor was taken from the GEOS-4 product (Suarez et al. 2005), and total column ozone from a blend of TOMS,

TOVS, and SMOBA. This release (Rel4-IP) of GLW features multiple changes to both inputs in atmospheric and cloud properties and algorithm. The algorithm incorporates the changes included with the LaRC Fu-Liou (Rose et al., 2013). Changes from ISCCP NNHIRS and ISCCP cloud properties were described in sections 3 and 4. This section describes additional changes to inputs and the LW algorithm relevant to SRB Rel4-IP including the addition of aerosols, cloud microphysical assumptions, trace gas total column and profile information and revised surface properties. The new flow is described in Figure 16.

5.1 Cloud microphysical property adjustments

Based on parameterizations introduced with ISCCP-H (Rossow 2017), the cloud particle sizes for both ice and water have been modified. The cloud particle sizes for ice clouds are now

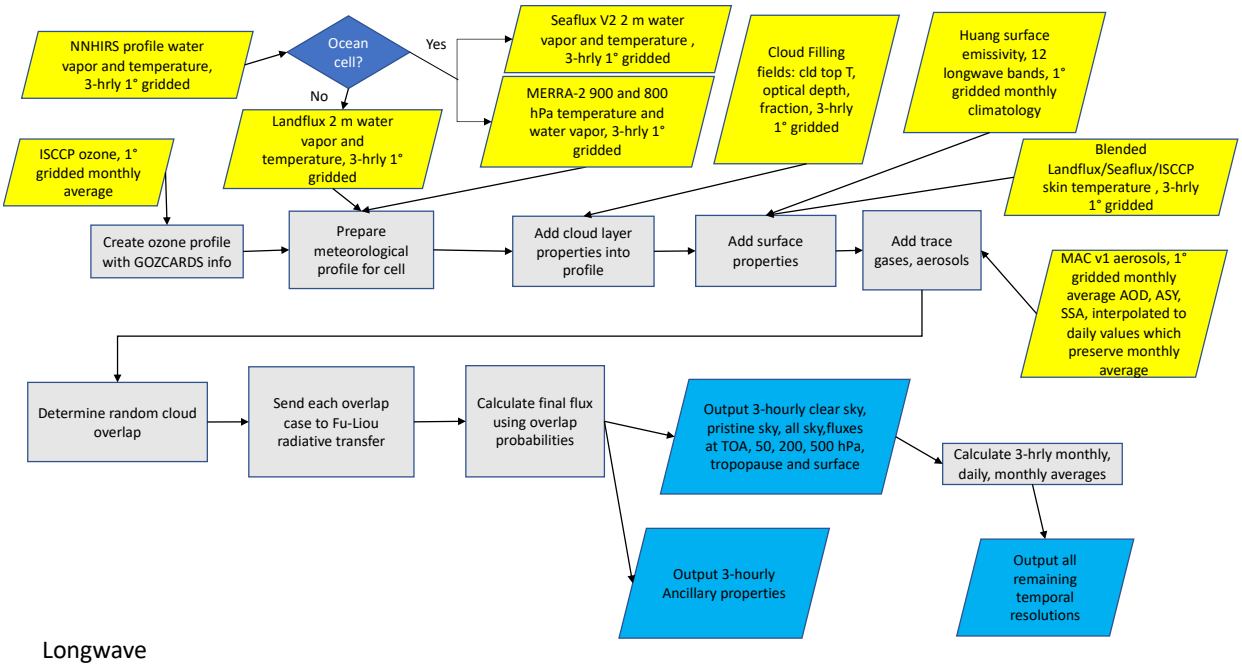

Figure 16. Flow diagram for SRB longwave algorithm.

based on the cloud optical depth (τ), with an effective radius of 20 um for optical depths less than 3.55 and 34μm for greater. As used in the GLW algorithm, based on Fu (1996) eq. 3.12, these become 52.35 and 30.79μm. This difference from ISCCP-D leads to different conversion factors for optical depth to water path, now being 7.0 for $\tau < 3.55$ and 11.9 for $\tau >= 3.55$. We then apply a correction ratio to account for the Fu-Liou bands. Liquid cloud particle sizes are differentiated by location over land or water, with the size being 13μm for the former and 15μm for the latter. These adjustments in turn alter the cloud liquid and ice water contents (CWC) which are passed to the flux algorithm. In previous SRB releases, the CWC were based on Fu and Liou (Fu et al. 1997, 1998) parameterizations for band 1 visible optical depth. In this release, not only is the optical depth VIS/IR ratio adjustment different, but the CWC are calculated from the conversion factors and corrections listed above. The changes are summarized in Table 1.

5.2 Surface skin temperature input changes

To construct the skin temperature field used in the GLW algorithm, Seaflux sea surface temperature (SST) Version 2 (Clayson et al. 2016a) and Princeton HIRS (Coccia et al. 2015) land surface temperature (LST), along with the ISCCP composite skin temperature (TSCOMP) from the processed cloud files are meshed. The Princeton HIRS LST (T_0, below) is corrected according to this equation:

$$T_s = B_{\Delta\upsilon}^{-1}\left\{\frac{1}{\varepsilon_{s_{\Delta\upsilon}}} B_{\Delta\upsilon}(T_o) - \left(\frac{1-\varepsilon_{s_{\Delta\upsilon}}}{\varepsilon_{s_{\Delta\upsilon}}}\right) L_{S_{\Delta\upsilon}}^{\downarrow}\right\}$$

B represents the Planck function integrated over the specified wavenumber range, T_o represents an equivalent skin temperature which corresponds to the correct amount of radiance leaving the surface, $\varepsilon_{s_{\Delta\upsilon}}$ is the surface emissivity for the wavenumber band, T_s is the actual skin temperature and $L_{S_{\Delta\upsilon}}^{\downarrow}$ is the downwelling radiance at the surface for the wavenumber.

The processed snow and ice field along with the new surface types are used to get an emissivity field for the 11 μm channel for the Plank inversion correction term. Based on a least-square polynomial fit between precipitable water (PW) and the longwave spectral flux at 11 μm, the following equation is used to estimate the downward longwave flux correction:

$$L_{S_{11\mu}}^{\downarrow} = aPW^3 + bPW^2 + cPW + d$$

For PW less than 25 kg m^{-2} the coefficients above are, in order: -0.000718564, 0.0363924, 0.504524, and -0.0506456. Greater than 25 kg m^{-2}, the coefficients are 0.000153379,-0.0284288, 2.28879, and -17.8094.

To complete the global skin temperature fields, the order of operations is the following:

1. If there is a valid LST for a grid box, the emissivity and flux corrected LST value is used.
2. If there is a valid SST and the grid box land percentage is less than 30% and the snow/ice coverage is less than 5%, then SST is used.
3. For any remaining grid box, TSCOMP is used.

Version	Criteria	Optical Depth	Cloud Water Content	R_e for radiative transfer
Rel4-IP	Ice cloud τ >=3.55	Day=ISCCP HX τ Night=35.0*0.376	$\tau * 11.9/Cld_{thick} * (1.0224/2.65957)$	52.35 µm
	Ice cloud τ <3.55		$\tau * 7.0/ Cld_{thick} * (1.0878/2.65957)$	30.79 µm
	Water cloud over land	Day= ISCCP HX τ Night=35.0*0.391	$\tau * 8.18/ Cld_{thick} * (1.16/2.55754)$	13 µm
	Water cloud over ocean		$\tau * 9.44/ Cld_{thick} * (1.16/2.55754)$	15 µm
Rel3.1	Ice cloud	Day=ISCCP DX water path Night=35.0*0.47	$\tau / (Cld_{thick} * (ap_{(1,1)} + ap_{(2,1)}/ R_e + ap_{(3,1)}/ R_e^2))$	60 µm
	Water cloud	Day=ISCCP DX water path Night=35.0*0.39	$\tau / (Cld_{thick} * (bz_{(j,1)}/ fl_j + (bz_{(j+1,1)}/ fl_{j+1} + (bz_{(j,1)} / fl_j) / (1.0/re_{j+1} - 1.0/re_j) * (1.0/R_e - 1.0/re_j))$, where j is the index for the appropriate R_e correspondence to the table re.	Low-level cloud = 9.84 µm Mid-level cloud = 6.16 µm

Table 1. Summary of optical depth (τ), cloud water content, and effective radius. CLDthick is the cloud thickness in meters. From the Fu-Liou tables and equations, re is effective radius, fl is the liquid water content, bz is the extinction coefficient, ap are empirical coefficients from the 1st Fu-Liou visible band.

5.3 Surface emissivity changes

Surface emissivity in Rel3.1 was based on the ISCCP static surface vegetation type which had no monthly variation. The only varying part of the emissivity field was based on the daily snow coverage. For Rel4-IP, surface emissivity comes from the Huang data set (Huang et al. 2016), which is gridded climatological monthly mean varying at each of the Fu-Liou longwave bands. A sample of the seasonal variation of the emissivity is shown in Figure 17. As with Rel3, these emissivities are modified by the daily snow amount when used in the radiative transfer calculations.

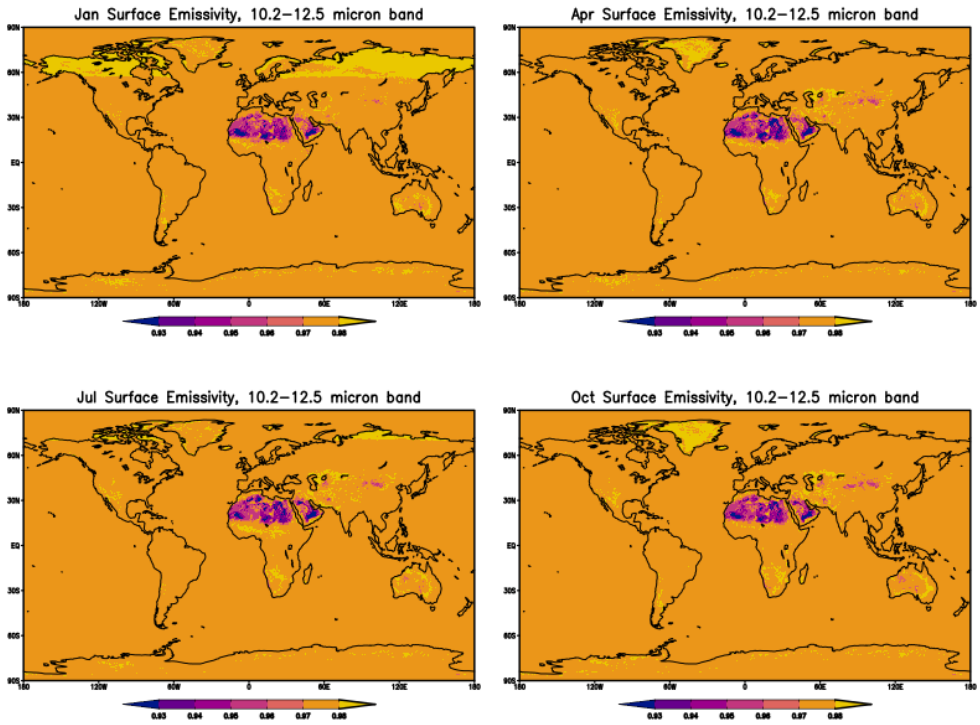

Figure 17. Mid-seasonal months showing the 10.2 to 12.5 μm band emissivity from Huang (2016).

5.4 Atmospheric profile changes

Due to using the NNHIRS meteorology, pressure levels at the very top of the atmospheric column are not present but are still needed to compute TOA fluxes. To compensate, the McClatchey et al., (1972) climatology have been reinstated from early versions. This extends the top-of-atmosphere (TOA) to 0.06 hPa in the tropics, 0.05 hPa in the mid-latitude winter, 0.07 hPa in the sub-arctic summer, and 0.04 in the sub-arctic winter. Because the lowest profile level to the surface is at 900 hPa, a surface minus 20 hPa level is added to the sounding by interpolation between the surface values and the 900 hPa values (if applicable).

Over oceans, the Seaflux Version 2 near-surface temperature and specific humidity data (Clayson et al. 2016b) are used in place of the NNHIRS meteorology and MERRA-2 (Modern Era Retrospective Analysis for Research and Applications) (Gelaro et al. 2017), replaces NNHIRS at 900 and 800 hPa. It was found that the NNHIRS did not adequately capture boundary level meteorology over the oceans.

5.4.1 Total column ozone abundance and ozone profiles

Total column ozone abundance is an ancillary product available with the ISCCP-H data series. TOMS, TOVS, SMOBA and OMI data are combined through regression fitting then spatially and temporally filled (Rossow 2017).

Ozone profiles for GLW are based on the GOZCARDS data files which give zonal merged ozone profiles for 25 pressure levels (Froidevaux et al. 2015). This replaces the Flemming profiles used in Rel3.1. Within the GLW algorithm, GOZCARDS data is interpolated to the pressure levels of the grid box meteorology and cloud data.

5.4.2 Trace/greenhouse gas amounts

GLW uses a monthly varying CO_2 concentration obtained from NOAA (ftp://aftp.cmdl.noaa.gov/products/trends/co2/). The concentrations of CH_4 and N_2O are constants of values 1.8 and 0.321 ppmv, respectively. CFC concentration is [268, 503 ,105] pptv for CFC-11, CFC-12 and CFC-22, respectively.

5.5 Addition of longwave aerosol optical properties

One major change from Rel3.1 is that aerosols have been included in this version. The wavelengths for the longwave algorithm have been processed from the MAC version 1 data. See Section 4 for more information on the MAC aerosols. The aerosols are distributed in the atmospheric profile by using the level fractions provided with the MAC data.

5.6 Revised cloud overlap procedure

The pre-processing code from Rel3.1 that prepares the meteorology and cloud overlap schemes has been modified to accept new inputs of meteorology and ancillary data. Because there is now an additional cloud type (high water), the cloud properties and overlap scheme subroutines have been modified to accommodate this additional type. There have been no modifications to the pressure thickness of the clouds assigned to any of the three layers (high, mid and low). High water clouds are assigned the same thickness as high ice. Corresponding to the ISCCP H changes, the maximum pressure for a cloud base has increased from 1000 hPa to 1025 hPa. The procedure for the random overlap now has 20 physically possible cases, up from the 16 that were used with the ISCCP DX clouds.

5.7 New products for longwave

5.7.1 Pristine sky fluxes

With the addition of MAC v1 aerosols to the calculation of longwave fluxes, the clear-sky fluxes now include aerosol effects, whereas in Rel3.1 they did not. Pristine-sky fluxes, which exclude both cloud and aerosol effects, are now available. These pristine-sky fluxes can be directly compared to Rel3.1 clear-sky fluxes. Aerosol radiative effect can be computed along with the cloud radiative effect.

5.7.2 Local sun time data products

In order to more directly match the shortwave flux products and to provide an additional choice for data users, there are now local sun time averaged fluxes available on the monthly and daily level. Many users in the building design and agriculture rely on local sun time data.

5.8 Sensitivity of fluxes to input and algorithm changes

This release of the GEWEX Longwave uses the LaRC Fu-Liou algorithm (Rose et al., 2013) for the radiative transfer. Release 3.1 longwave used a slightly older version of the same algorithm. Sensitivity tests from the annual average of 2007 have shown that the surface pristine-sky (clear-sky for Rel3.1) surface downward flux has the largest algorithm change of +2.9 W m^{-2} for the global average. The Pristine OLR change is much smaller, at -0.36 W m^{-2}.

5.8.1 Flux sensitivity to changes in clouds and meteorology

In order to evaluate the effects of changing from DX to HX clouds and changing from GEOS-4 to NNHIRS meteorology, two exploratory runs were made. Both use the same algorithm as the official version and the same ancillary inputs. One version used the ISCCP DX

clouds with NNHIRS meteorology (including Seaflux and Landflux 2-meter temperature and humidity), while the other used DX and GEOS-4 meteorology (not including Seaflux and Landflux). Both versions used the surface skin temperature of the official version. With the combination of these two versions and the official version, we can isolate the flux differences brought about by the change of either cloud or meteorology.

Figure 18 demonstrates that each component (clouds and meteorology) contributes roughly equally to the global flux difference but with different regional effects.

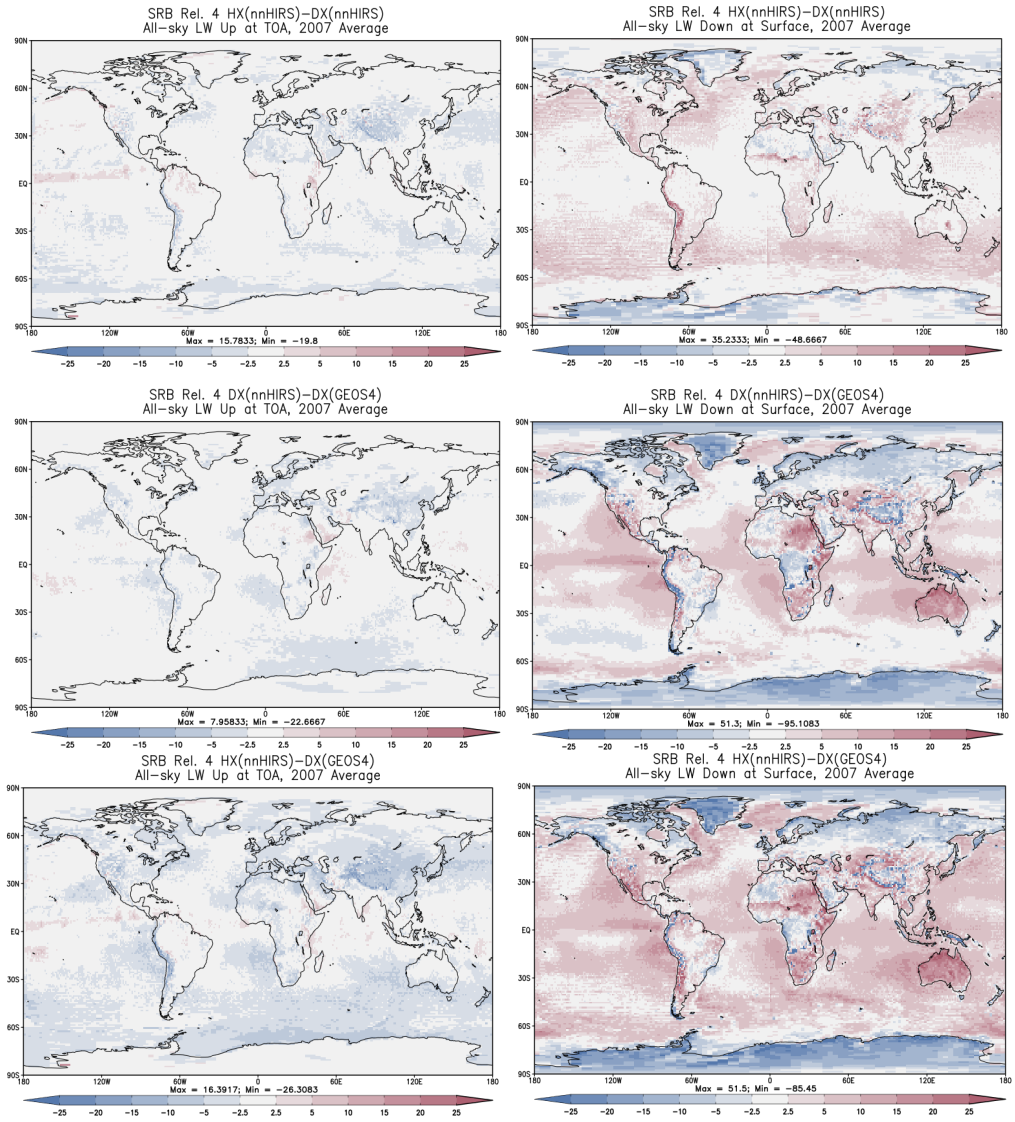

Figure 18. Contrasts differences in the annual averaged 2007 radiative fluxes for the all-sky TOA LW up (left panels) and surface downward LW flux (right panels) for 3 sets of conditions: 1) Top panels show the flux differences due to using the new cloud properties relative to the Rel3 DX cloud properties using the NNHIRS atmospheric profiles 2) middle panels show the flux differences due just to changes between the NNHIRS and GEOS4 atmospheric profiles and 3) bottom panels show the flux differences between using the new clouds and atmospheric profile vs the clouds and atmospheric profile from Rel3.

5.8.2 Contrast between Rel 3 and Rel4-IP radiative flux components

The overlapping time period between Rel4-IP and Rel3.1 for global coverage occurs from January 1988 to December 2007. In this section we explore the global areal average differences between the two versions. Select map differences are shown in Figure 19, while Table 2 contains the global and tropical (20°N-20°S) areal averages.

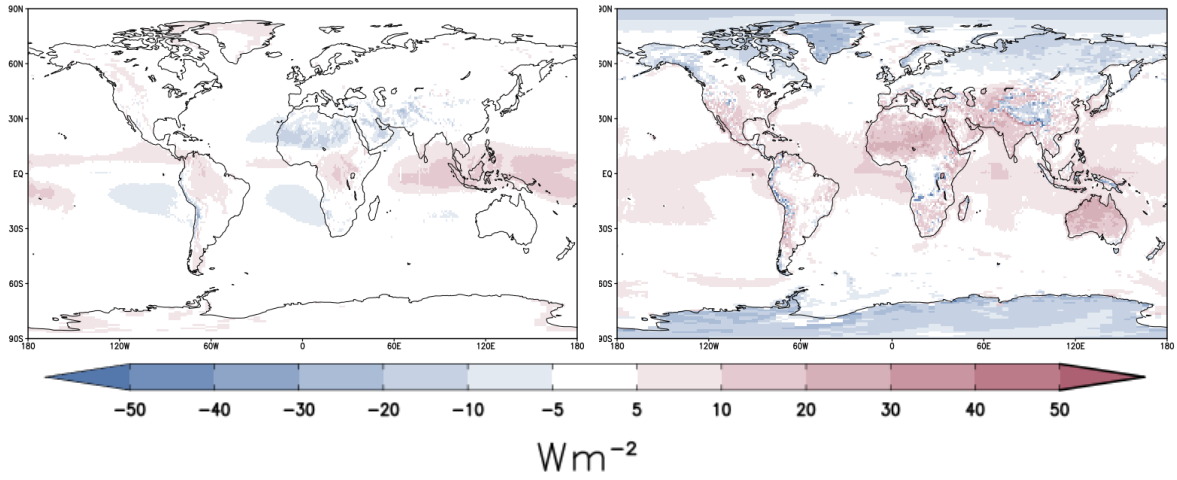

Figure 19. Maps showing the difference in the longwave all-sky TOA and surface fluxes between Rel4-IP and Rel3.1 for the over-lapping time period from January 1988 through December 2007. left is TOA Up (OLR), right is downward surface

The global annual average difference in TOA fluxes (OLR) for the overlapping time period compared with Rel3.1 is 1.27 W m^{-2}. Clear-sky OLR is less than Rel3.1 with a difference of -3.10 W m^{-2}, which gives a TOA cloud radiative effect difference of -4.27 W m^{-2}. The difference between the pristine sky Rel4-IP OLR and the Rel3.1 clear-sky (which did not include aerosols) is -1.81 W m^{-2}.

The global average difference for all-sky surface down is 3.10 W m^{-2}. In this case, the tropics contribute strongly to the positive difference and the polar regions mediate the global number by having a negative difference. Clear-sky differences are 4.75 W m^{-2}, giving a cloud radiative effect difference of -1.65 W m^{-2}. Comparing pristine-sky Rel4-IP to clear-sky Rel3.1 gives a difference of 3.34 W m^{-2}.

Because of the different skin temperature input sources, the upward surface flux is quite different from Rel3.1. The global annual average of Rel4-IP is 1.93 W m^{-2} higher, with land surfaces contributing greatest to the difference.

		TOA Up		Sfc Down		Sfc Up		Sfc Net	
Sky Condition	Area	Rel3.1	Rel4-IP	3.1	4-IP	3.1	4-IP	3.1	4-IP
All-sky	Global	238.0	239.3	344.0	347.1	396.5	398.5	-52.6	-51.4
All-sky	Tropical	256.5	259.2	404.0	410.4	457.7	459.6	-53.7	-49.2
Clear-sky/ Pristine-sky	Global	265.2	262.1/ 263.4	310.7	315.5 /314. 1	396.5	398.5		
Clear-sky/ Pristine-sky	Tropical	286.3	283.6/ 284.8	383.0	391.0 /389. 7	457.7	459.6		

Table 2. Longwave flux global and tropical (20°N-20°S) areal averages for the time period of 1988-2007 for Rel3.1 and Rel4-IP.

5.8.3 Validation against surface measurements

The surface measurement comparisons between Rel3.1 and Rel4-IP are shown in the validation tables below. Table 3 compares the surface downward longwave flux to the Baseline Surface Radiation Network (BSRN) measurements for the overlapping time between the two versions of GLW. For all measures of statistical comparisons, Rel4-IP has slightly worsened. As seen in section 5.8.1, changes in both meteorology and clouds have led to increased downward radiation. Table 4, which compares the downward surface flux to the ocean buoy observations from the Pacific Marine Environmental Laboratory (PMEL), shows similar results as BSRN, although there are slight improvements in 3-hourly and daily correlation coefficients and standard deviations. Extended validation for Rel4-IP is continued in section 7.4.1.2.

BSRN Longwave Surface Site Validation for January 1992 through December 2007							
Version	Time Scale	Bias	RMS	ρ	σ	μ_{DATA}	N
Rel3.1	3-Hourly	0.2	29.9	0.92	29.86	313.9	1090559
	Daily	-0.1	21.2	0.96	21.23	315.4	130172
	3-Hourly-Monthly	-1.4	15.5	0.98	15.39	308.6	39041
	Monthly	-0.7	11.2	0.99	11.23	308.4	4863
Rel4-IP	3-Hourly	1.7	32.9	0.91	32.82	315.4	1090559
	Daily	1.4	25.3	0.94	25.25	316.8	130172
	3-Hourly-Monthly	0.1	19.1	0.97	19.13	310.1	39041
	Monthly	0.8	15.9	0.98	15.89	309.9	4863

Table 3. Surface downward longwave BSRN validation comparison of GLW Rel3.1 and Rel4-IP for the 1992 through 2007 time period.

PMEL Longwave Surface Site Validation for January 2000 through December 2007							
Version	Time Scale	Bias	RMS	ρ	σ	μ_{DATA}	N
Rel3.1	3-Hourly	-1.6	17.8	0.78	17.7	403.5	77291
	Daily	-1.6	12.7	0.87	12.6	403.5	9713
	3-Hourly-Monthly	-1.4	7.8	0.94	7.7	404.2	2215
	Monthly	-1.6	6.6	0.96	6.4	404.0	290
Rel4-IP	3-Hourly	4.4	17.2	0.81	16.6	409.4	77291
	Daily	4.4	12.8	0.88	12.1	409.4	9713
	3-Hourly-Monthly	4.6	9.4	0.93	8.2	410.2	2215
	Monthly	4.4	7.9	0.96	6.6	409.9	290

Table 4. Surface downward longwave PMEL validation comparison of GLW Rel3.1 and Rel4-IP for the 2002 through 2007 time period.

5.9 Extension of LW before 1988 and after 2009

Because the input data sets of Seaflux and Landflux do not extend through the entire ISCCP-H record (Figure 1), the main longwave data set release is limited to 1988 through 2009. Seaflux is available through the end of the ISCCP-H record and Landflux is available from the beginning of the record. A separate land-only longwave product from July 1983 through December 1987 and an ocean-only product from January 2010 through June 2017 have therefore been made available. Each of these uses the same algorithm as the main product and input assumptions as appropriate.

6 Shortwave Algorithm Changes

6.1 Summary of SW algorithm changes

The core of the Rel3 shortwave algorithm is based on the methodology described in Pinker and Laszlo (1992). The Rel4-IP shortwave algorithm features multiple changes to both inputs and algorithm, with revisions to spectral bands, ocean surface albedo, and adjustments for snow and ice surfaces. The processing flow is described in Figure 20.

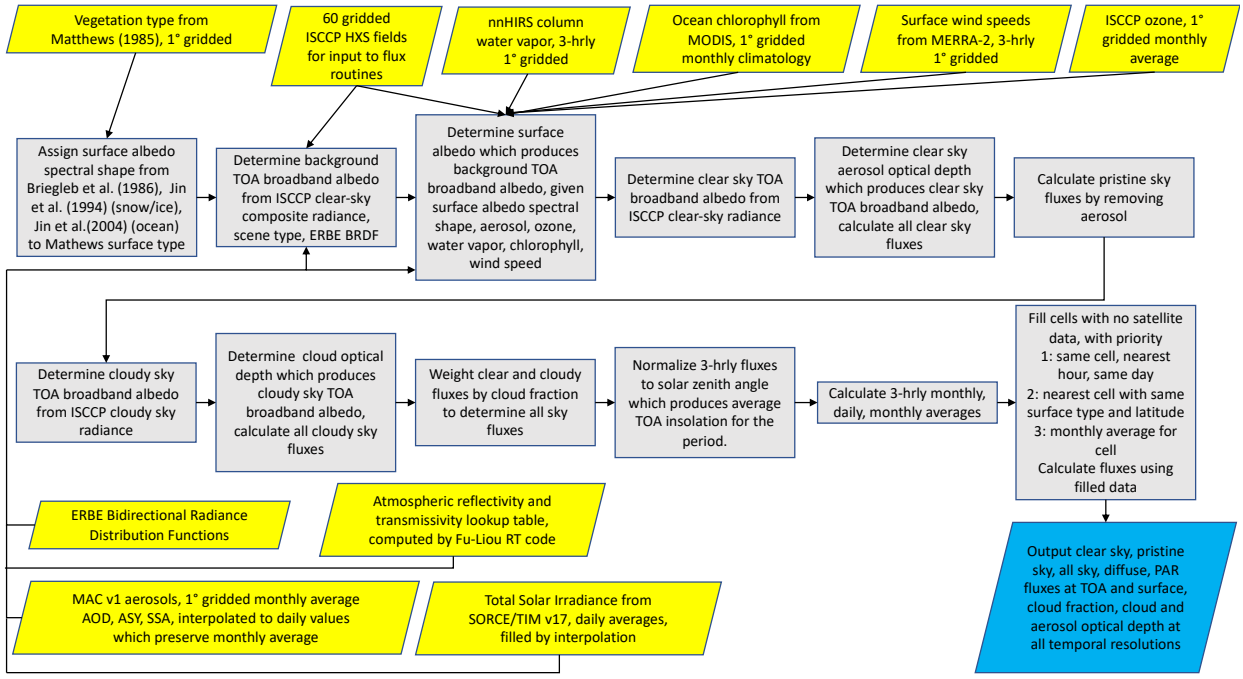

Figure 20. Flow diagram for SRB shortwave algorithm.

6.1.1 Revised spectral bands

The GSW model uses lookup tables of spectral atmospheric transmissivities and reflectivities based on a range of input values (atmosphere or cloud optical depth, cosine solar zenith angle, column water vapor, column ozone, surface elevation). For Rel3, the tables are generated using the delta-Eddington method for five spectral bands (200-300, 300-400, 400-500, 600-700, and 700-4000nm). Clouds are assumed to be liquid, and aerosols are either a generic maritime or generic continental. Rel4-IP recalculates the lookup tables using the Fu and Liou (1992) algorithm as modified by the CERES group (Rose et al. 2013). There are now 18 bands (Table 5). Cloud phase is now included, so separate tables for liquid (10µm effective radius) and ice cloud (60µm effective radius) are generated. Aerosol now includes asymmetry parameter and single scattering albedo as inputs, with the MACv1 dataset providing monthly values of each, allowing a continuous range of aerosol composition (homogenous mixture assumed).

6.1.2 Revised ocean surface albedos

The spectral albedo of ocean has been changed from Rel3 which used Briegleb et al. (1986) for ocean albedo, which varied direct reflectance with sun angle only. Rel4-IP has adopted the scheme of Jin et al. (2004) which incorporates wind speed, aerosol optical depth, and chlorophyll concentration. Wind speed is taken from NNHIRS, aerosol optical depth from MACv1, and chlorophyll from the monthly MODIS climatology (Werdell and Bailey 2005). Sample changes in ocean albedo are shown in Figure 21. The new schema gives a much lower ocean albedo at shallow sun angles. There is now spectral variation with a higher albedo at visible wavelengths and lower albedo in the near infrared.

Band 1	Band 2	Band 3	Band 4	Band 5	Band 6	Band 7	Band 8	Band 9
175-225	225-244	244-286	286-298	298-322	322-358	358-438	438-498	498-595

Band 10	Band 11	Band 12	Band 13	Band 14	Band 15	Band 16	Band 17	Band 18
595-690	690-794	794-889	889-1042	1042-1410	1410-1905	1905-2500	2599-3509	3509-4000

Table 5. Spectral bands treated in GSW Rel4-IP algorithm, in μm.

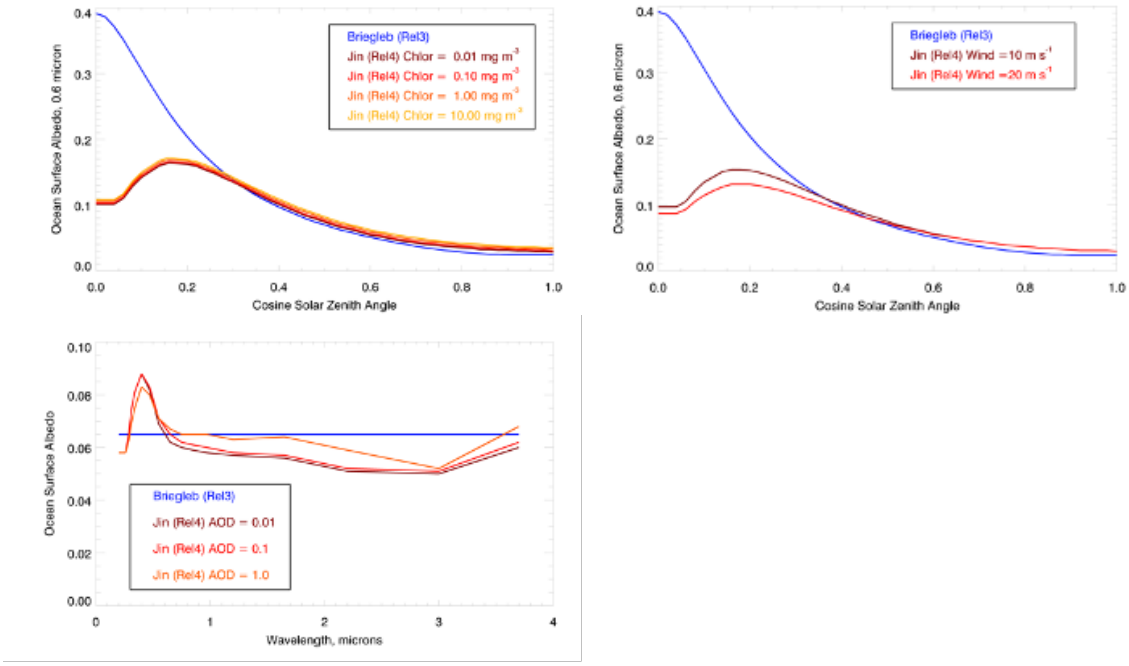

Figure 21. Changes in surface albedo in Rel4-IP. Top left: Variation with solar zenith angle and chlorophyll. Top right: Variation with solar zenith angle and wind speed. Bottom left: Spectral shape.

6.1.3 Adjustments for snow/ice surfaces

Snow and ice spectral albedos have been changed, from the Warren and Wiscombe (1980) approach in Rel3, to Jin (1994). The Rel3 approach treated all snow and ice the same, whereas the Rel4-IP (Figure 22) approach differentiates snow (generally brighter) from ice (generally darker).

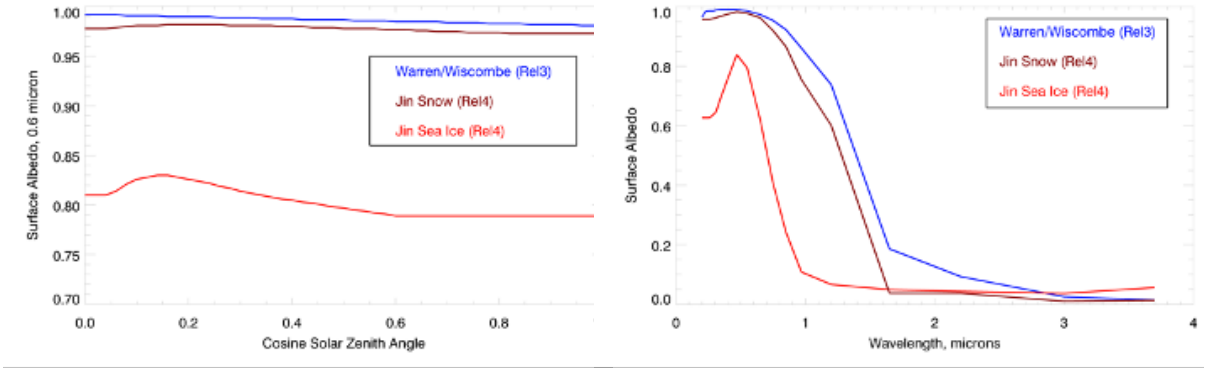

Figure 22. Rel4-IP changes in snow/ice albedo. Left: variation of snow and sea ice albedo with zenith angle. Right: Spectral shape of snow and sea ice albedo.

6.1.4 New total solar irradiance

Total Solar Irradiance in Rel3 was fixed at 1367 W m^{-2}. Rel4-IP uses the daily time series from SORCE/TIM v17 (Kopp and Lean, 2011), with gaps filled by linear interpolation. Values vary within ~1 W m^{-2} around a mean of ~1360.8 W m^{-2} (Figure 23).

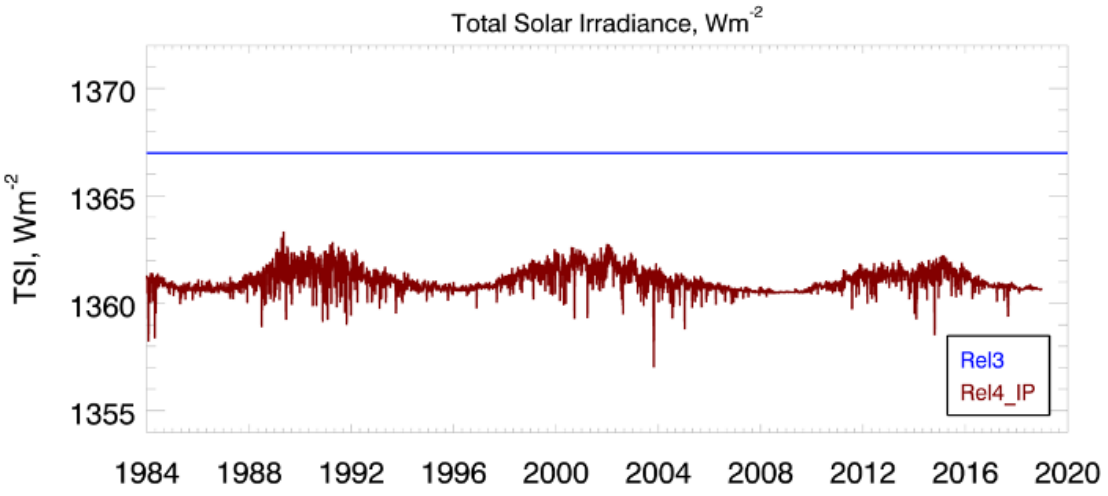

Figure 23. Total Solar Irradiance. Rel3 is a constant 1367 W m-2. Rel4-IP varies daily around a lower mean.

6.2 Sensitivity of fluxes to algorithm and input changes

6.2.1 Contrast between Rel 3 and Rel4-IP radiative flux components

The net result for the years 1984-2007 of all the input changes is a global reduction of 1.3 W m^{-2} in reflected TOA shortwave radiation, and a global reduction of 3.3 W m^{-2} in shortwave radiation reaching the surface (Figure 24 and Table 6). The surface reduction occurs primarily over the oceans, with the land surfaces showing a substantial increase. Several factors go into the overall changes. First, the radiative transmission is lower in the new radiative transfer

algorithm. This reduces both surface downward and TOA upward fluxes. Second, the input aerosol is more realistic, and generally produces lower optical depths over the land, leading to higher transmission there. Third, the new ISCCP HX clouds generally favor lower cloud fractions over ice, but higher cloud optical depth, reducing surface fluxes there. Fourth, the reduction in overall Total Solar Irradiance reduces all fluxes.

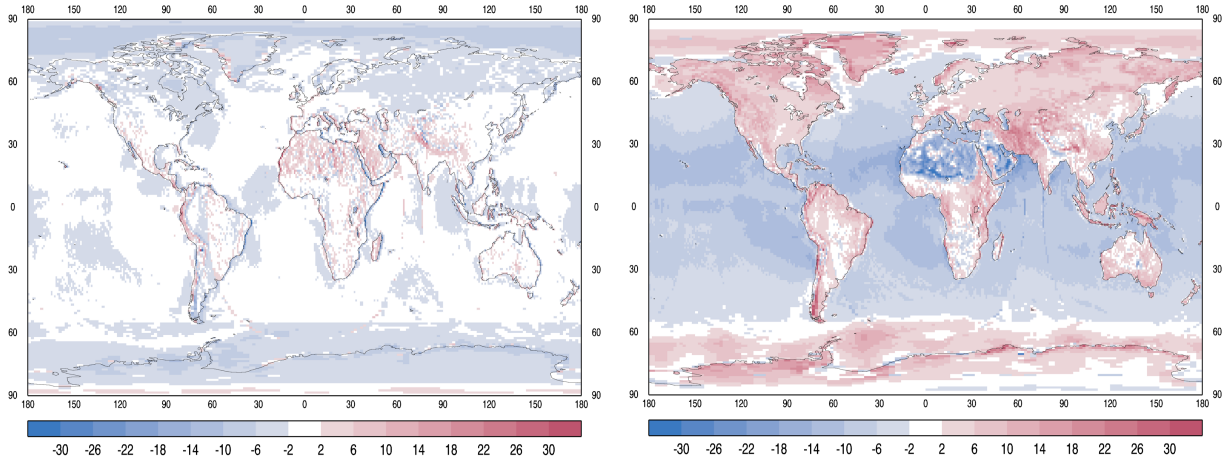

Figure 24. Shortwave flux changes in SRB from Rel3 to Rel4-IP, 1984-2007 averages. Left: TOA Upward Flux. Right: Surface Downward Flux.

6.2.2 Validation against surface measurements

Validation of surface downward flux against ground measurements is given in the tables below, as compared to the previous release. Biases over both land (Table 6) and water (Table 7) have improved for each time scale between Rel3 and Rel4-IP. There are slight improvements in the RMS and standard deviation over land, while the ocean buoy values for these are similar to the same from the previous version. Validation against the full range of data is presented in section 7.3.

BSRN Shortwave Surface Site Validation for January 1992 through December 2007							
Version	Time Scale	Bias	RMS	ρ	σ	μ_{DATA}	N
Rel3	3-Hourly	-7.8	86.6	0.95	86.2	278.9	592612
	Daily	-1.3	30.3	0.96	30.3	164.8	69182
	3-Hourly-Monthly	-3.4	26.6	0.99	26.4	130.5	28299
	Monthly	-3.7	17.3	0.98	16.9	165.7	2662
Rel4-IP	3-Hourly	-2.7	77.1	0.96	77.5	283.8	592862
	Daily	1.5	27.7	0.97	27.7	167.8	69098
	3-Hourly-Monthly	-1.0	24.1	0.99	24.1	132.8	28352
	Monthly	-0.8	14.2	0.99	14.2	168.5	2662

Table 6. Surface downward shortwave BSRN validation comparison of GSW Rel3 and Rel4-IP for the 1992 through 2007 time period.

PMEL Shortwave Surface Site Validation for January 2000 through December 2007							
Version	Time Scale	Bias	RMS	ρ	σ	μ_{DATA}	N
Rel3	3-Hourly	14.6	94.5	0.96	93.4	397.2	250946
	Daily	9.1	34.5	0.87	33.3	246.8	48826
	3-Hourly-Monthly	8.8	29.2	1.00	27.8	244.7	12574
	Monthly	8.8	15.1	0.95	12.4	246.7	1564
Rel4-IP	3-Hourly	1.4	95.5	0.96	95.5	383.9	251054
	Daily	0.9	34.7	0.85	34.7	238.6	48826
	3-Hourly-Monthly	0.7	26.0	1.00	26.0	236.6	12574
	Monthly	0.6	12.6	0.95	12.6	238.5	1564

Table 7. Surface downward shortwave PMEL validation comparison of GSW Rel3 and Rel4-IP for the 2000 through 2007 time period.

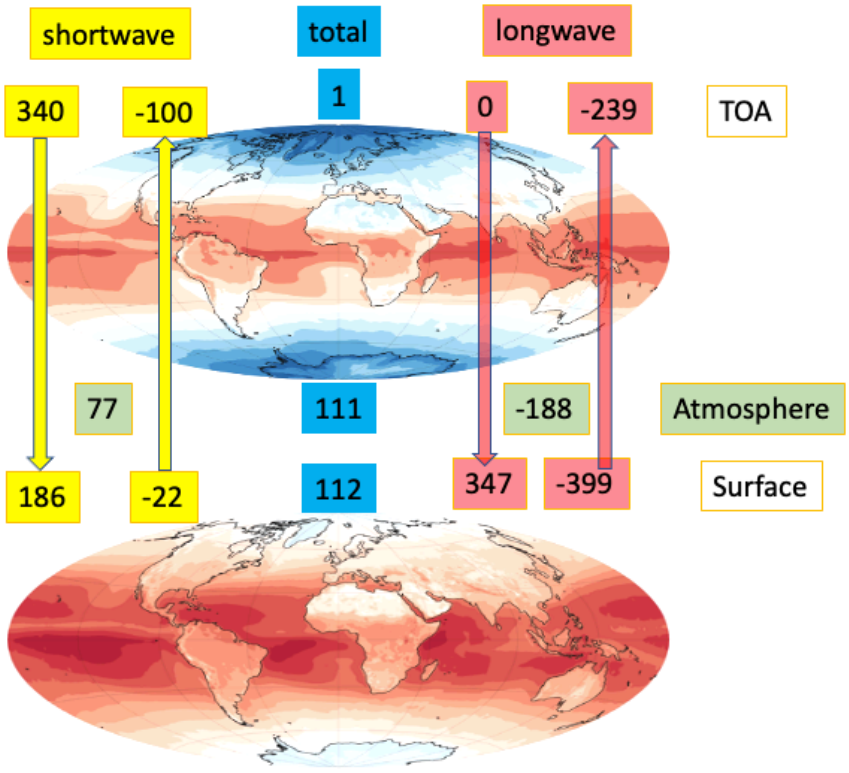

Figure 25. Schematic of the global energy balance from Rel4-IP for January 1988 through December 2009. All values in W m-2.

7 SRB Rel4-IP TOA and Surface Flux Assessment

7.1 Global energy budget

Combining the shortwave and longwave fluxes into a global energy budget gives good agreement with the values given by (Wild et al. 2015) despite the usage of two different algorithms to compute the fluxes. A visual representation of the flux components and the total flux for Rel4-IP is given in the diagram in Figure 25. These globally averaged numbers from January 1988 through December 2009 are all within the uncertainty range proposed in (Wild et al. 2015) and summarized in Table 8.

Level	Flux Component	Wild et al (2015) SW	Wild et al (2015) LW	Level	Flux Comp.	Wild et al (2015) SW	Wild et al (2015) LW
Surface	Down	185 (179:189)	342 (338:348)	TOA	Down	340 (340:341)	0
	Up	25 (22:26)	398 (394:400)		Up	100 (96:100)	239 (236:242)
	Net	160 (154:166)	-56 (-46:-62)		Net	240 (240:245)	-239 (-236:-242)
				Whole Atmos.	Net	80 (74 :91)	-183 (-174:-196)

Table 8. Individual flux component averages from Wild et al. 2015 for the global energy balance with the uncertainty range in parentheses.

As another way of considering the global energy budget and how it compares to similar data sets, a Taylor diagram has been constructed for Figure 26. A Taylor diagram allows for a quick, visual comparison of important statistics. In this figure, CERES EBAF 4.1 (Loeb et al. 2018) is used as the reference data set, with a normalized standard deviation and correlation coefficient computed for the comparison data sets. In using EBAF 4.1 as the reference, a plotted point on the diagram at a normalized standard deviation of 1.0 and a correlation of 1.0 would represent a

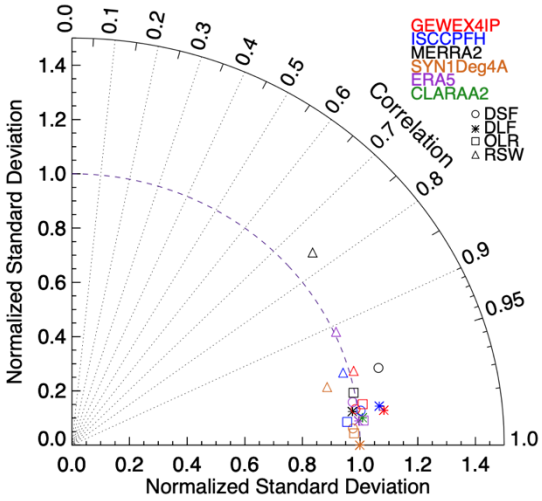

Figure 26. Taylor diagram of the upward fluxes at TOA and the downward fluxes at surface, with the reference set to CERES EBAF 4.1 for the January 2001 to December 2009 time period.

perfect statistical match. SRB Rel4-IP does well in the comparison, with downward surface longwave flux and upward TOA shortwave flux being the least like EBAF. Compared with the other considered models, Rel4-IP performs well in this regard. Bias values associated with the diagram are given in Table 9.

Flux bias relative to EBAF 4.1				
Data Set	SW TOA Up (RSW)	LW TOA Up (OLR)	SW Sfc Down (DSF)	LW Sfc Down (DLF)
GEWEX Rel.4-IP	1.0	-0.8	-1.0	1.8
ISCCP FH	5.0	-8.2	-2.9	-7.0
MERRA-2	6.7	-1.8	-0.7	-13.0
SYN 1Deg	2.0	-2.1	-2.8	2.2
ERA5	-1.7	1.8	1.3	-5.6
CLARA A2				-2.7

Table 9. Biases of the models/data sets presented in Figure 26 as compared to the reference set, EBAF 4.1 for January 2001 through December 2009.

7.2 TOA Fluxes

7.2.1 Shortwave comparisons and variability

Comparisons of global averaged reflected shortwave fluxes at TOA are given in Table 10. Rel4-IP is generally within 1 W m^{-2} of EBAF for all sky and clear sky reflected fluxes, and TOA cloud radiative effect. Agreement with SYN1DEG is within 3 W m^{-2}. Rel4-IP is closer to the CERES products than are the other flux products given, ERA5, ISCCP FH, and MERRA-2.

2001-2009	Rel.4-IP	EBAF 4.1	SYN 1Deg 4A	ERA5	ISCCP FH	MERRA-2
TOA Up All-sky	100.21	99.24	101.20	97.58	104.27	105.98
TOA Up Clear-sky	53.46	53.90	51.54	51.35	55.21	51.45
TOA Up Pristine-sky	48.51		46.54			47.99
TOA CRE	46.75	45.81	49.66	46.23	49.06	54.54

Table 10. Table of long-term January 2001 to December 2009 annual average shortwave TOA fluxes for Rel4-IP, EBAF Ed.4.1, SYN 1Deg 4A, ERA5, ISCCP FH and MERRA-2.

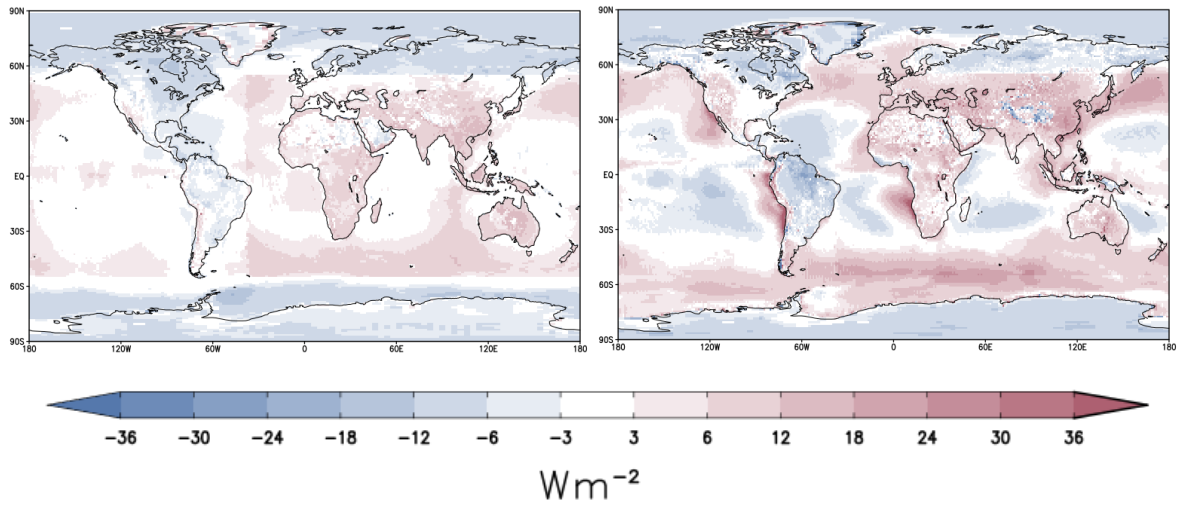

Figure 27. Shortwave TOA upward flux difference in the 2001-2009 average, between CERES EBAF (left) and ECMWF ERA5 (right).

A map of the Rel4-IP-EBAF differences in all-sky TOA upward flux is given in Figure 27. A strong pattern is seen of Rel4-IP being higher than EBAF in the tropics and midlatitudes, and of being lower in the high latitudes. This appears to correlate somewhat with the ISCCP satellite coverage, with geostationary satellites covering the 55°S-55°N region and polar orbiters poleward from there.

Global timeseries of SW TOA upward flux anomalies of Rel3, Rel4-IP, EBAF, and SYN1Deg are given in Figure 28. The anomalies are computed relative to a base period of 2001-2007, which is the period shared by all four products. Variability of the two GSW products is considerably higher than the CERES products, though much of the excess GSW variability is seen in the pre-2000 period, before the beginning of the CERES period. Rel4-IP shows a stronger Pinatubo effect (1991-1995) than Rel3. The increase of Rel3 reflected flux after 2005 is known to be an ISCCP D series calibration artifact which has been corrected in the H series and therefore also in GSW Rel4-IP. This can also be seen in the 12-month running mean of 60°S-60°N TOA reflected flux (Figure 29). This plot also shows the ERBE values from 1985-1998, which generally agree fairly well with the GSW products, and include the Pinatubo perturbation.

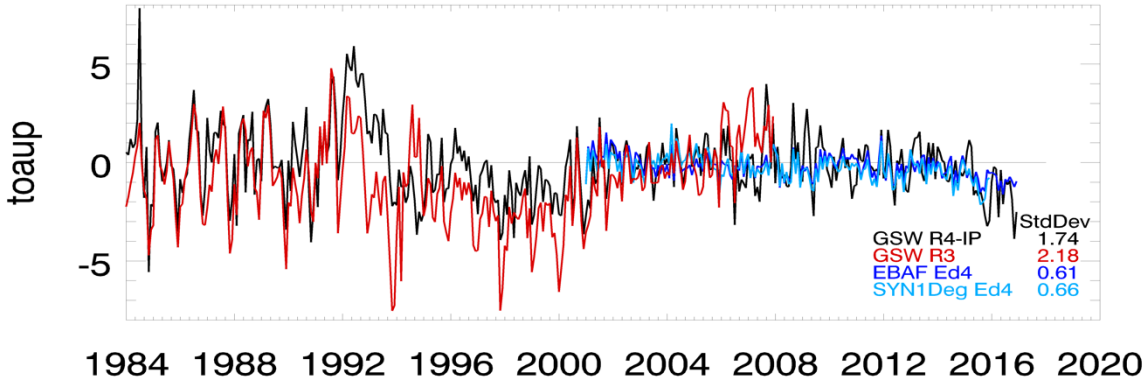

Figure 28. All-sky shortwave TOA Up global monthly anomaly timeseries for years 1984-2017, relative to a 2001-2007 baseline. Rel4-IP is shown as the black line, Rel3 is in red, EBAF 4.1 is dark blue and SYN 1Deg Ed. 4A is light blue.

7.2.2 Longwave comparisons and variability

Table 1 gives the global averaged fluxes for the outward longwave fluxes at TOA for a common period from January 2001 through December 2009. Since EBAF all-sky OLR is based on satellite observations, it is considered a standard with which to compare. Rel4-IP all-sky OLR is within the 1 W m^{-2} uncertainty given by the EBAF 4.1 data quality summary. While the clear-sky component is 3.7 W m^{-2} lower than the EBAF value, it is still within the clear-sky flux uncertainty of 5 W m^{-2}. Pristine-sky outward flux compares well with SYN1Deg.

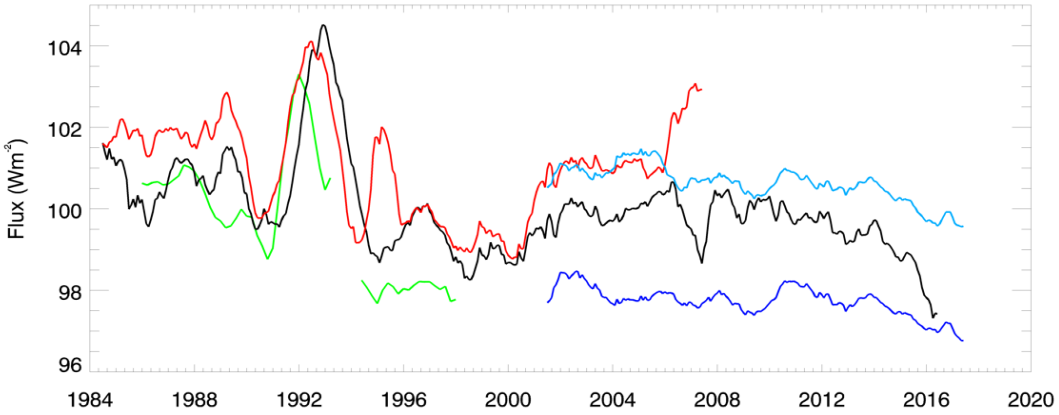

Figure 29. All-sky shortwave TOA Up 12-month running mean for 60°N to 60°S average. Rel4-IP is shown as the black line, Rel3 is in red, EBAF 4.1 is dark blue, and SYN 1Deg Ed. 4A is light blue. The ERBE Ed. 4 72-day mean is green.

2001-2009	Rel.4-IP	EBAF 4.1	SYN 1Deg 4A	ERA5	ISCCP FH	MERRA-2
TOA Up All-sky	239.45	240.22	238.13	242.05	232.02	238.47
TOA Up Clear-sky	262.53	266.18	262.44	264.00	259.07	267.35
TOA Up Pristine-sky	263.81		262.90			267.55
TOA CRE	23.07	25.96	24.31	21.95	27.05	28.88

Table 11. Table of long-term January 2001 to December 2009 annual average longwave TOA fluxes for Rel4-IP, EBAF Ed.4.1, SYN 1Deg 4A, ERA5, ISCCP FD and MERRA-2.

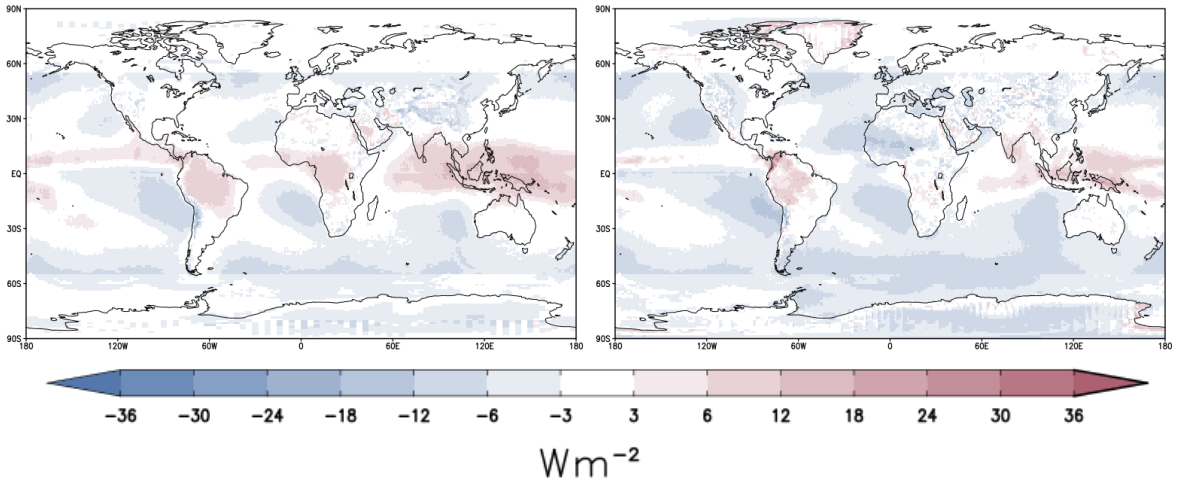

Figure 30. Longwave TOA upward flux difference in the 2001-2009 average, between CERES EBAF (left) and ECMWF ERA5 (right).

While the overall global averages compare well with EBAF 4.1, it can be seen in the map difference in OLR (Figure 30) that there are significant regional biases. Rel4-IP OLR in tropical regions between 15°N/S tends to have larger values than EBAF but beyond the tropics it is less than EBAF. The combination of these helps the global average to be much closer than it might be otherwise. Comparing the map of Rel4-IP OLR with the reanalysis model from ERA5 shows many of the same features as the map with EBAF, but with fewer areas in the tropics where Rel4-IP is greater. Clear-sky map differences with EBAF are almost uniformly negative (EBAF greater than Rel4-IP) indicating that the inherent meteorology is either cooler and/or less moist in Rel4-IP. The effect of clouds added to the atmosphere creates the positive bias in the tropics.

Timeseries analysis shown in Figures 31 and 32 shows good agreement with CERES products. Rel4-IP is capturing the variability of the OLR well. The 12-month running mean also shows how Rel4-IP is within the two CERES products.

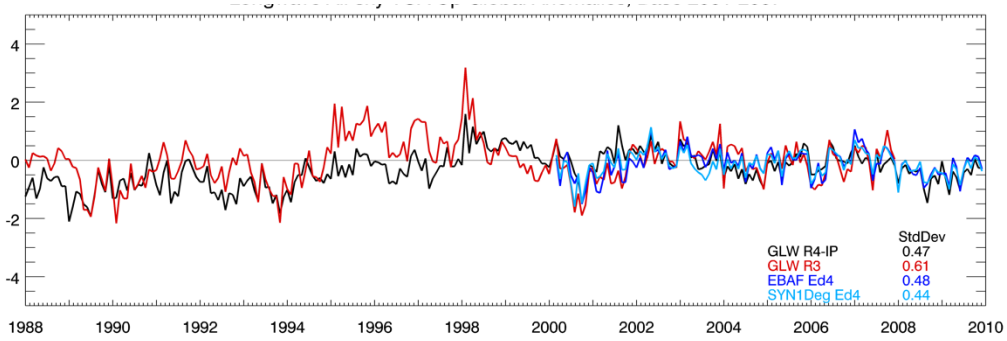

Figure 31. All-sky TOA Up global monthly anomaly timeseries for the base years 2001-2007. Rel4-IP is shown as the black line, Rel3.1 is in red, EBAF 4.1 is dark blue and SYN 1Deg Ed. 4A is light blue.

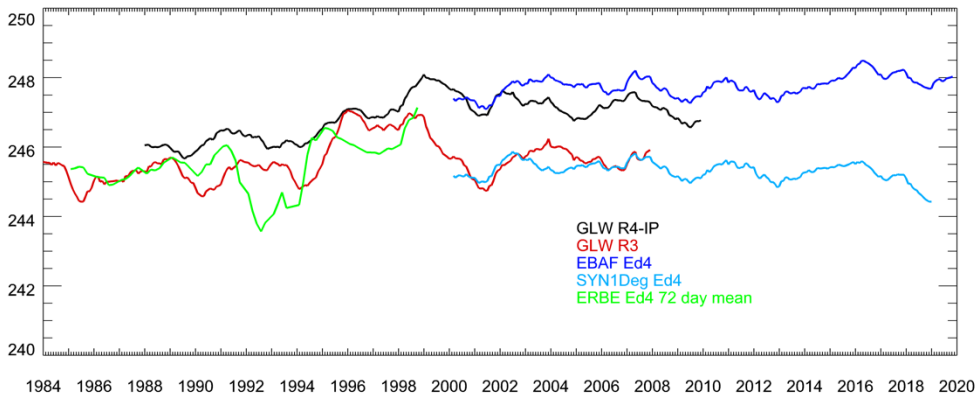

Figure 32. All-sky TOA Up 12-month running mean for 60°N to 60°S average. Rel4-IP is shown as the black line, Rel3.1 is in red, EBAF 4.1 is dark blue, and SYN 1Deg Ed. 4A is light blue. The ERBE Ed. 4 72-day mean is green.

7.2.3 Total net comparisons and variability

Because total net flux at TOA is the sum of the shortwave net TOA flux and the negative OLR, many of the spatial characteristics seen in the upward components of the longwave and shortwave fluxes from the previous sections are seen in the maps in Figure 33. Longwave patterns tend to dominate 45° N to 45°S, with shortwave fluxes enhancing the effects. Shortwave tends to dominate the polar regions. The timeseries analysis (Figure 34) again shows good agreement in the variability with CERES.

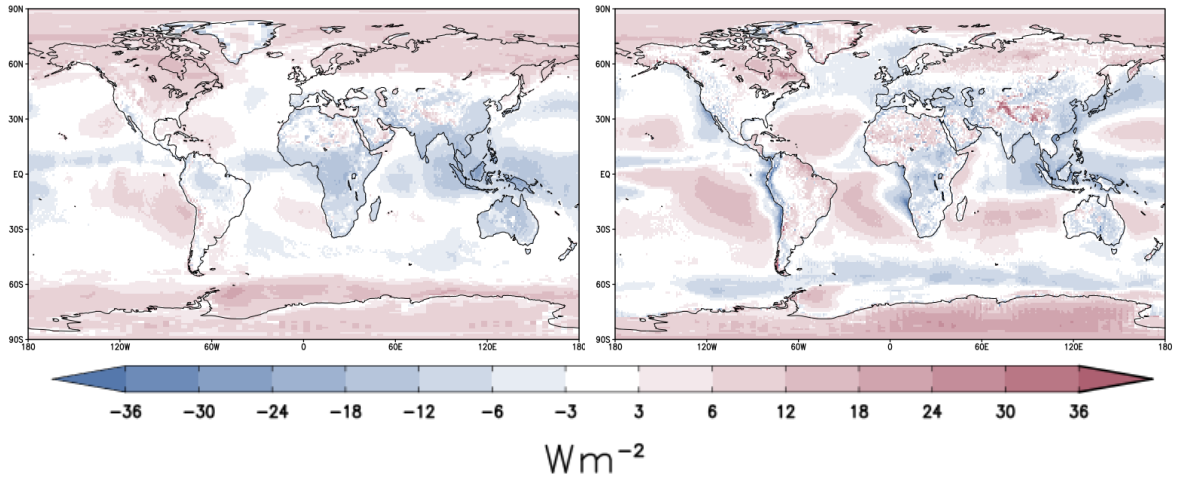

Figure 33. TOA total net (SW+LW) flux difference between Rel.4-IP and EBAF 4.1 (left) and Rel.4-IP and ERA5 (right) for the common over-lapping period of each.

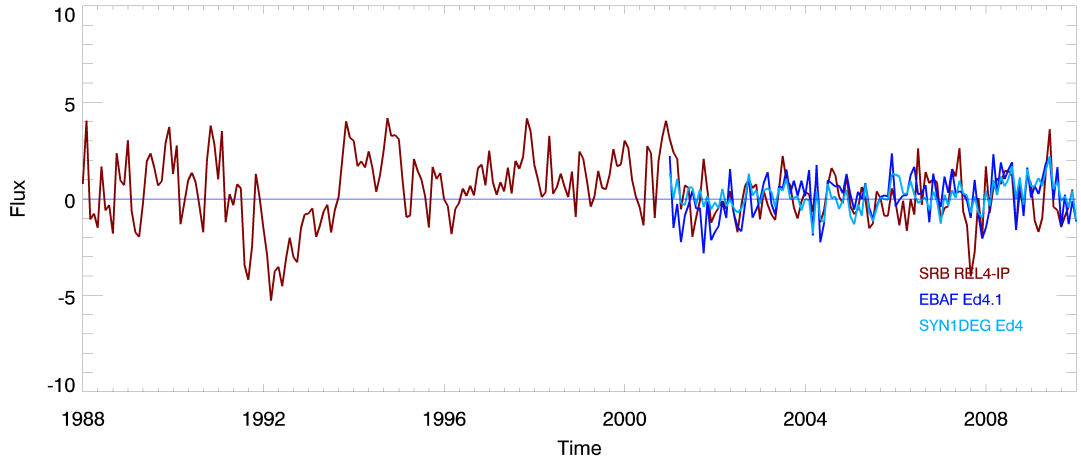

Figure 34. TOA total net global monthly anomaly timeseries for the base years 2001-2007. Rel4-IP is shown as the red line, EBAF 4.1 is dark blue and SYN 1Deg Ed. 4A is light blue.

7.3 Surface fluxes

The Rel4-IP shortwave and longwave fluxes have been validated against the Baseline Surface Radiation Network (BSRN) data and the Pacific Marine Environmental Laboratory (PMEL) buoy data. As of this writing, there are 12,116 site-months of BSRN data from 73 sites and 6235 buoy-months of PMEL data. The global distribution of these sites is shown in Figure 35. The original BSRN data are 1-, 2-, 3- or 5-minute intervals. Ohmura et al. (1998) gave information about how BSRN started and what had been achieved up till then. The PMEL shortwave total fluxes are from pyranometer. Rutan et al. (2015) has more information about PMEL data. Additional background information about PMEL data is available in Bourlès et al. (2008) and McPhaden et al. (2009, 1998).

The 3-hourly, daily and monthly mean validation statistics are given in tables that follow. Note that shortwave 3-hourly validations include only daytime values, which is why their biases are roughly two times larger than their daily and monthly counterparts which, by definition, include nighttime, or zero, values.

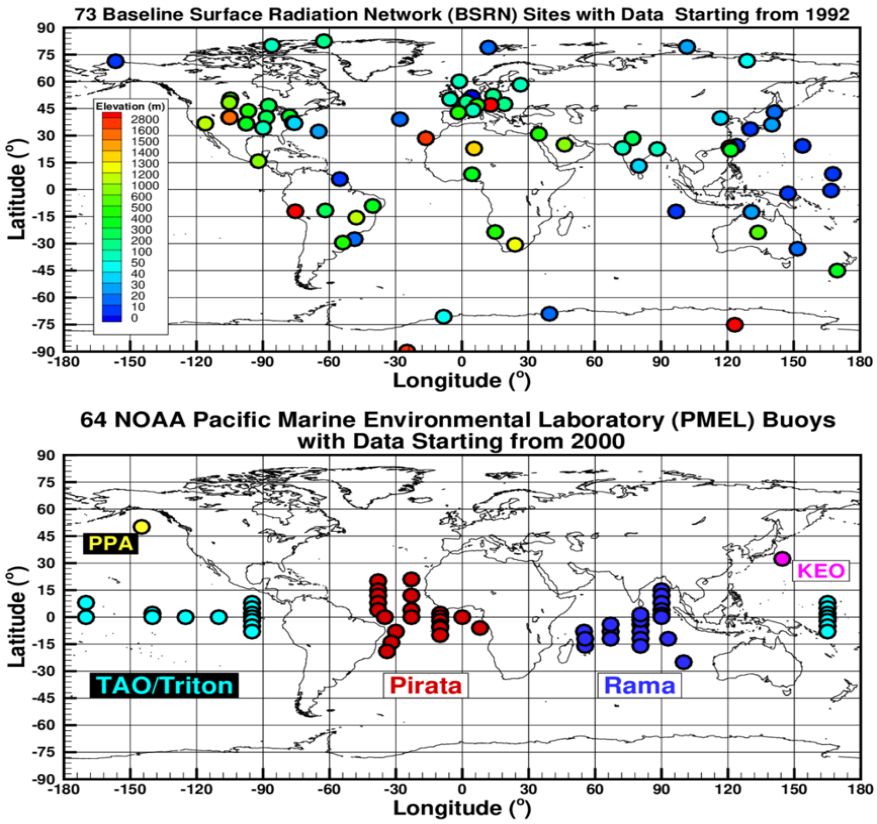

Figure 35. Surface-based observation sites. Top panel shows the 73 Baseline Surface Radiation Network (BSRN) sites on all seven continents. The lower panel shows the 64 Pacific Marine Environmental Laboratory (PMEL) buoys deployed.

7.3.1 Shortwave comparisons and variability

Globally averaged shortwave surface flux fields from 2001-2009 (Table 12) show that Rel4-IP is generally within 3 W m^{-2} of EBAF and SYN1Deg, with similar good agreement with the ERA5, ISCCP-FH, and MERRA-2 flux products. However, maps of the Rel4-IP differences with EBAF and SYN1Deg (Figure 36) show that there are compensating differences producing the global agreement. In particular, Rel4-IP is much lower over the Sahara compared to both products, and much higher than SYN1Deg in the coverage area of the GOES satellites, the Americas, the western Atlantic, and the eastern Pacific.

Validation statistics of Rel4-IP compared to BSRN ground sites are given in Table 13 and Figure 37. Biases at the different time scales are within 3 W m^{-2} of zero. Root mean square (RMS) differences reduce as the period of averaging increases. Ocean validation with PMEL buoys is shown in Figure 37 and Table 14. Biases there are generally positive but within 5 W m^{-2} of zero. The timeseries of both land and ocean validation show no strong temporal signal.

Timeseries comparison with EBAF and SYN1Deg surface fluxes and surface albedo (Figure 38) show results similar to the TOA results discussed in Section 7.2.1: overall agreement is good, with SRB products showing higher variability than CERES products.

Global annual average fluxes for January 2001 through December 2009						
	Rel.4-IP	EBAF 4.1	SYN 1Deg	ERA5	ISCCP FH	MERRA-2
Sfc Down All-sky	185.9	186.9	184.1	188.1	184.0	186.1
Sfc Down Clear-sky	241.1	241.1	242.7	242.6	242.3	242.1
Sfc Down Pristine-sky	252.8		253.1			248.5
Sfc Up All-sky	22.2	23.3	22.5	24.3	24.6	23.2
Sfc Up Clear-sky	28.5	29.6	28.5	30.0	31.2	30.3
Sfc Net All-sky	163.7	166.0	163.7	163.8	159.4	162.9
Sfc CRE	-55.2	-54.3	-58.6	-54.5	-58.3	-56.0

Table 12. January 2001-December 2009 annual average shortwave surface fluxes for Rel4-IP, EBAF Ed 4.1, SYN1Deg 4A, ERA5, ISCCP FH, and MERRA-2.

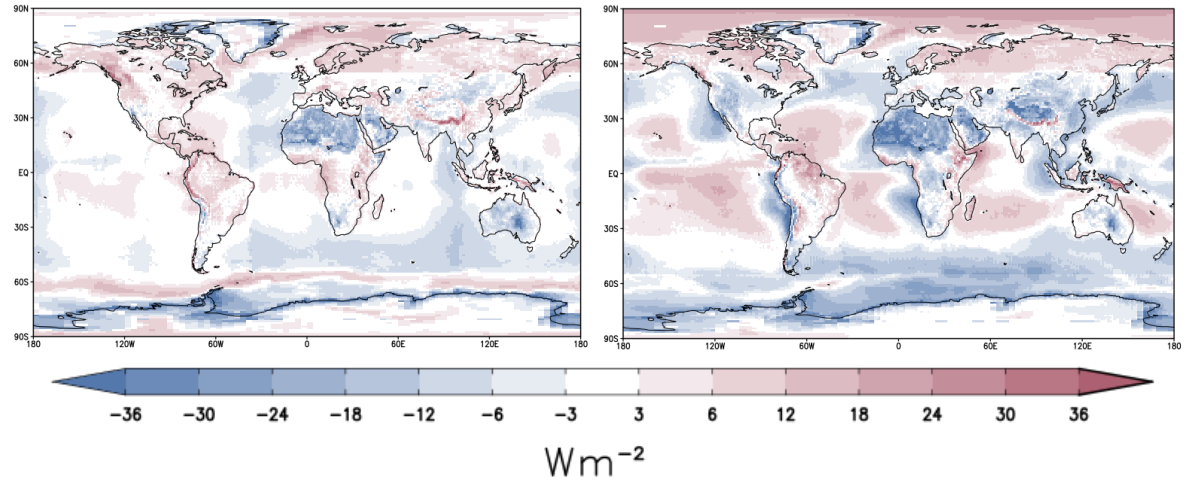

Figure 36. Shortwave surface downward flux, 2001-2007 average, difference from CERES EBAF (left) and CERES SYN1DEG (right).

GEWEX SRB GSW(Rel4-IP)-BSRN January 1992 through June 2017						
Time Scale	Bias	RMS	ρ	σ	μ_{DATA}	N
3-Hourly	-2.9	77.6	0.96	77.5	285.4	1280023
Daily	1.3	28.1	0.97	28.1	170.5	154459
3-Hourly-Monthly	-1.1	24.2	1.00	24.2	139.7	62108
Monthly	-1.0	14.7	0.99	14.7	170.1	6097

Table 13. GEWEX SRB surface shortwave downward flux validation against BSRN data over the period 1992-2017.

GEWEX SRB GSW(Rel4-IP)-PMEL January 2000 through June 2017						
Time Scale	Bias	RMS	ρ	σ	μ_{DATA}	N
3-Hourly	4.9	95.0	0.96	94.9	381.0	648515
Daily	3.1	34.6	0.86	34.4	236.3	126578
3-Hourly-Monthly	2.8	28.3	1.00	28.2	231.2	32159
Monthly	2.9	13.9	0.95	13.6	234.8	4158

Table 14. GEWEX SRB surface shortwave downward flux validation against PMEL data over the period 2000-2017.

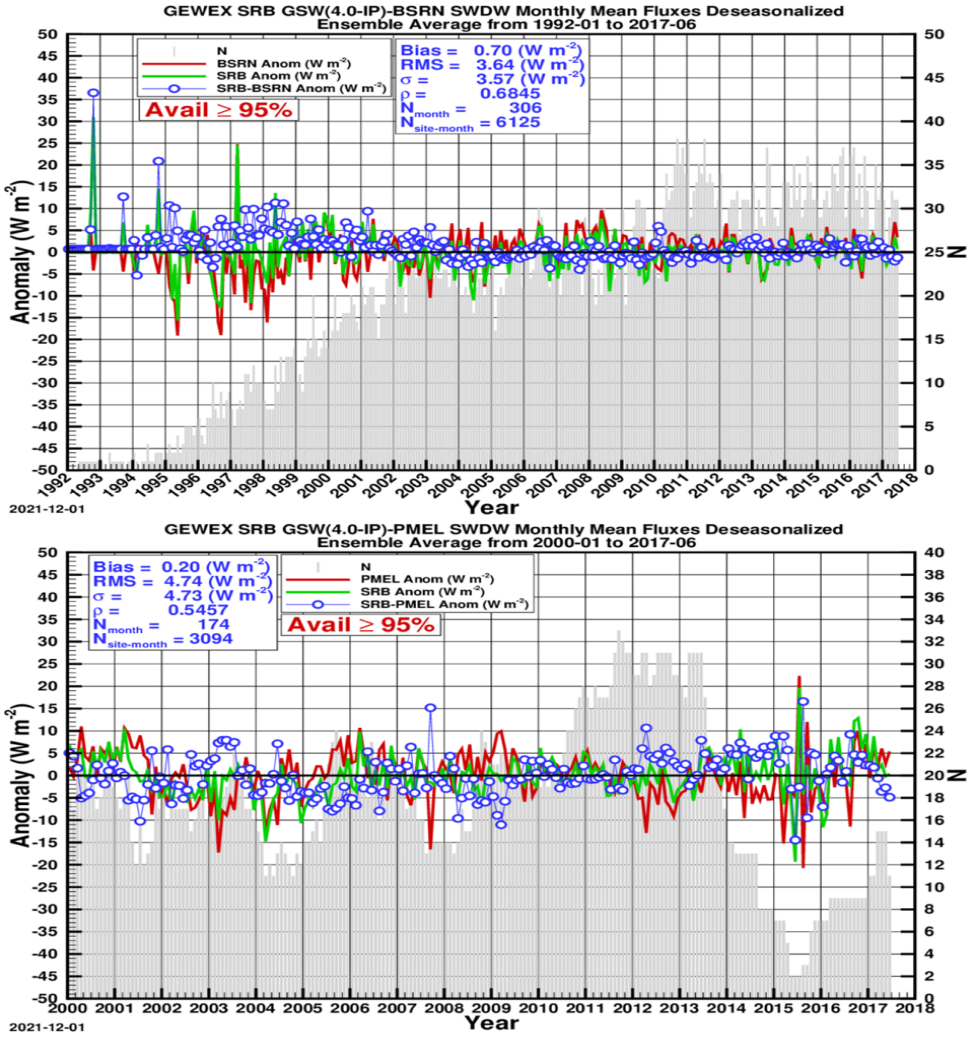

Figure 37. Comparisons of time series of ensemble average. The top panel shows the time series of the ensemble average of the BSRN monthly mean shortwave downward flux and Rel.4.-IP counterpart. The lower panel is the same as the upper panel except the comparison is with the PMEL buoy data.

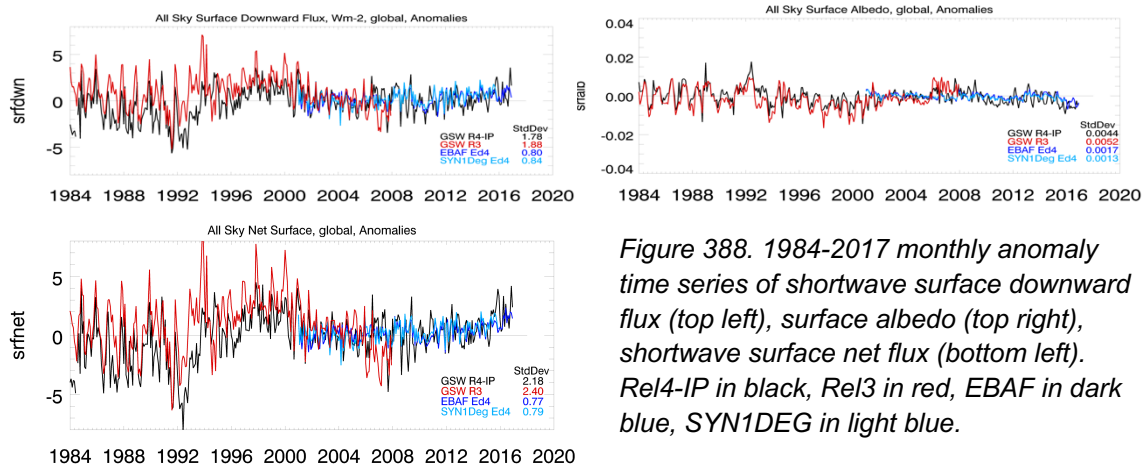

Figure 388. 1984-2017 monthly anomaly time series of shortwave surface downward flux (top left), surface albedo (top right), shortwave surface net flux (bottom left). Rel4-IP in black, Rel3 in red, EBAF in dark blue, SYN1DEG in light blue.

7.3.2 Longwave comparisons and variability

Longwave downward surface site validation for all available data is presented in Table 15, Table 16 and Figure 39. This expands on the smaller subset in the earlier section comparing with Rel3.1. Land validation against BSRN stations shows good comparisons with the overall bias, but the RMS is higher than desired. As is typical, the RMS decreases and the correlation coefficient increases as the averaging level increases. Validation against the ocean buoys in the PMEL data again illustrates the higher ocean fluxes in Rel4-IP associated with clouds and meteorology.

Global averages for longwave surface fluxes compared to various satellite and reanalysis products are given in Table 17. Rel4-IP compares well to all, generally being in the middle of those presented. However, the map differences comparing to EBAF and ERA5 (Figure 40) show that positive and negative regions off-set each other to create a global average that is closer. The map differences exhibit many of the same patterns as shown in Figure 18, which explores the flux changes due to clouds and/or meteorology. Timeseries variability (Figure 41) for Rel4-IP again shows good agreement with the CERES products and improvements from Rel3.1.

Rel4-IP BSRN Longwave Surface Site Validation January 1992 through December 2009						
Time Scale	Bias	RMS	ρ	σ	μ_{DATA}	N
3-Hourly	1.8	32.7	0.91	32.7	316.0	1307985
Daily	1.5	25.2	0.94	25.1	317.3	156069
3-Hourly-Monthly	0.4	19.0	0.97	19.0	311.0	46962
Monthly	0.9	15.9	0.98	15.9	309.9	5835

Table 15. Surface downward longwave BSRN validation comparison of GLW Rel4-IP for the 1992 through 2009 time period.

Rel4-IP PMEL Longwave Surface Site Validation January 2000 through June 2017						
Time Scale	Bias	RMS	ρ	σ	μ_{DATA}	N
3-Hourly	3.4	18.6	0.84	18.3	405.4	343510
Daily	3.4	13.8	0.91	13.3	405.4	43116
3-Hourly-Monthly	4.6	10.3	0.96	9.2	405.2	9047
Monthly	3.2	9.2	0.96	8.7	402.9	1393

Table 16. Surface downward longwave PMEL validation comparison of Rel4-IP for the Jan. 2000 through June 2017 time period.

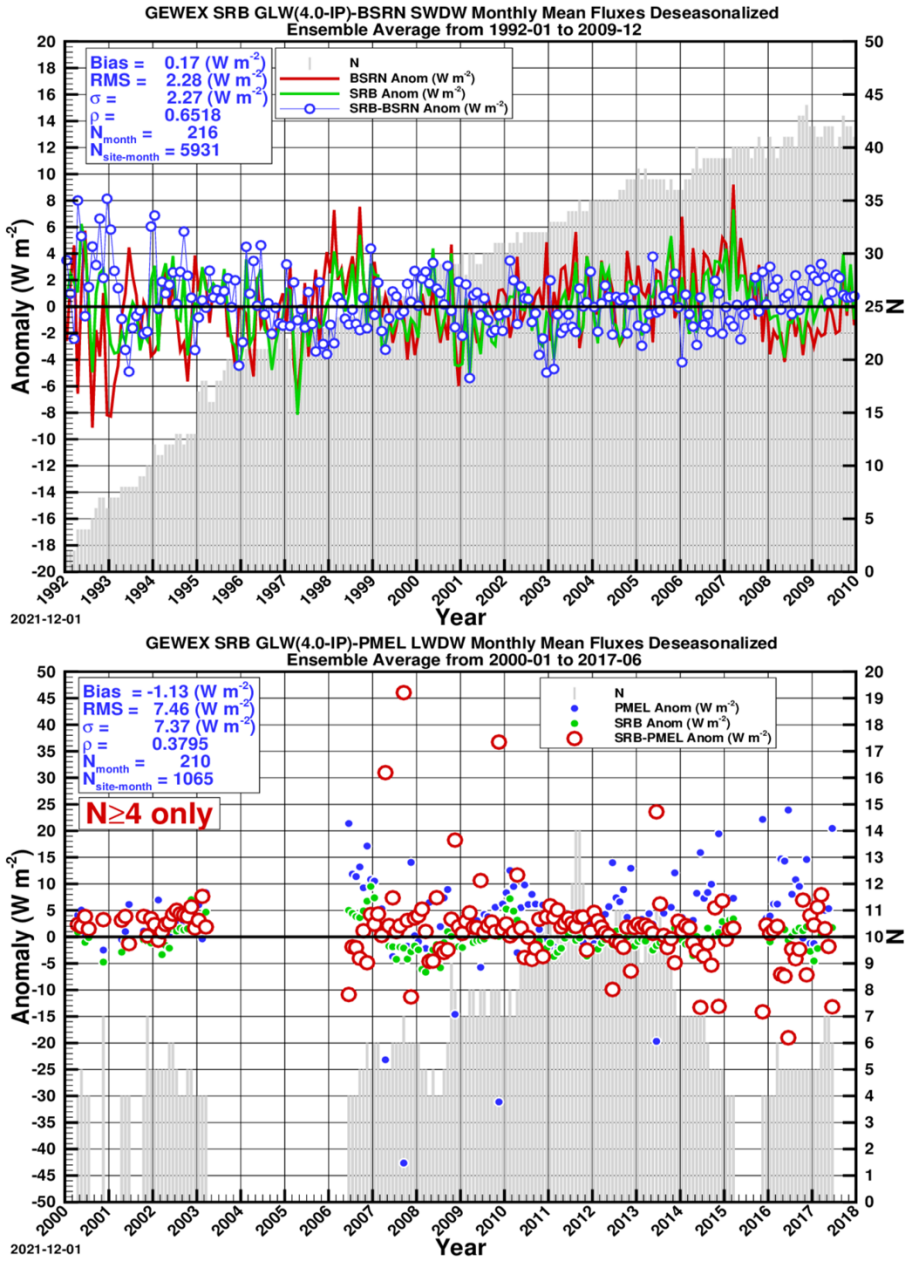

Figure 39. Comparisons of time series of ensemble average. The top panel shows the time series of the ensemble average of the BSRN monthly mean longwave downward flux and its Rel.4-IP counterpart. The lower panel is the same as the upper panel except the comparison is with PMEL buoy data.

Global annual average fluxes for January 2001 through December 2009						
Flux Parameter	Rel.4-IP	EBAF 4.1	SYN 1Deg	ERA5	ISCCP FH	MERRA-2
Sfc Down All-sky	346.9	345.1	347.3	339.6	338.1	332.2
Sfc Down Clear-sky	316.2	317.4	317.7	314.5	314.8	310.1
Sfc Down Pristine-sky	314.8		316.0			308.8
Sfc Up All-sky	399.3	398.6	398.0	397.5	392.5	394.0
Sfc Up Clear-sky	398.4		397.3	397.1	390.6	
Sfc Net All-sky	-52.3	-53.4	-50.0	-57.9	-54.4	-61.9
Sfc CRE	30.8	27.8	29.6	24.7	23.3	22.0

Table 17. Table of long-term January 2001 to December 2009 annual average longwave surface fluxes for Rel4-IP, EBAF Ed.4.1, SYN 1Deg 4A, ERA5, ISCCP FH and MERRA-2.

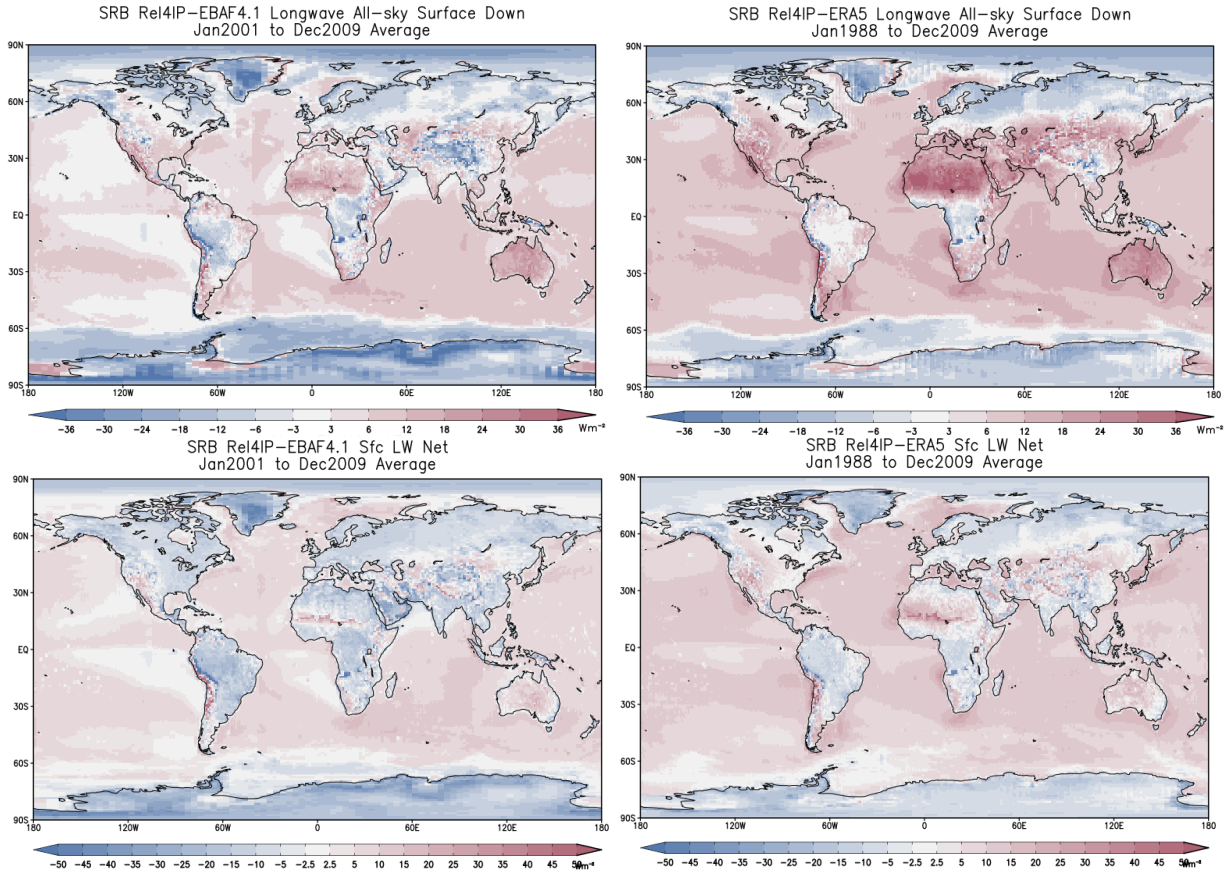

Figure 40. Surface longwave flux difference between Rel.4-IP and EBAF 4.1 (left) and Rel.4-IP and ERA5 (right), downward (top) and net (bottom) for the common overlapping period of each.

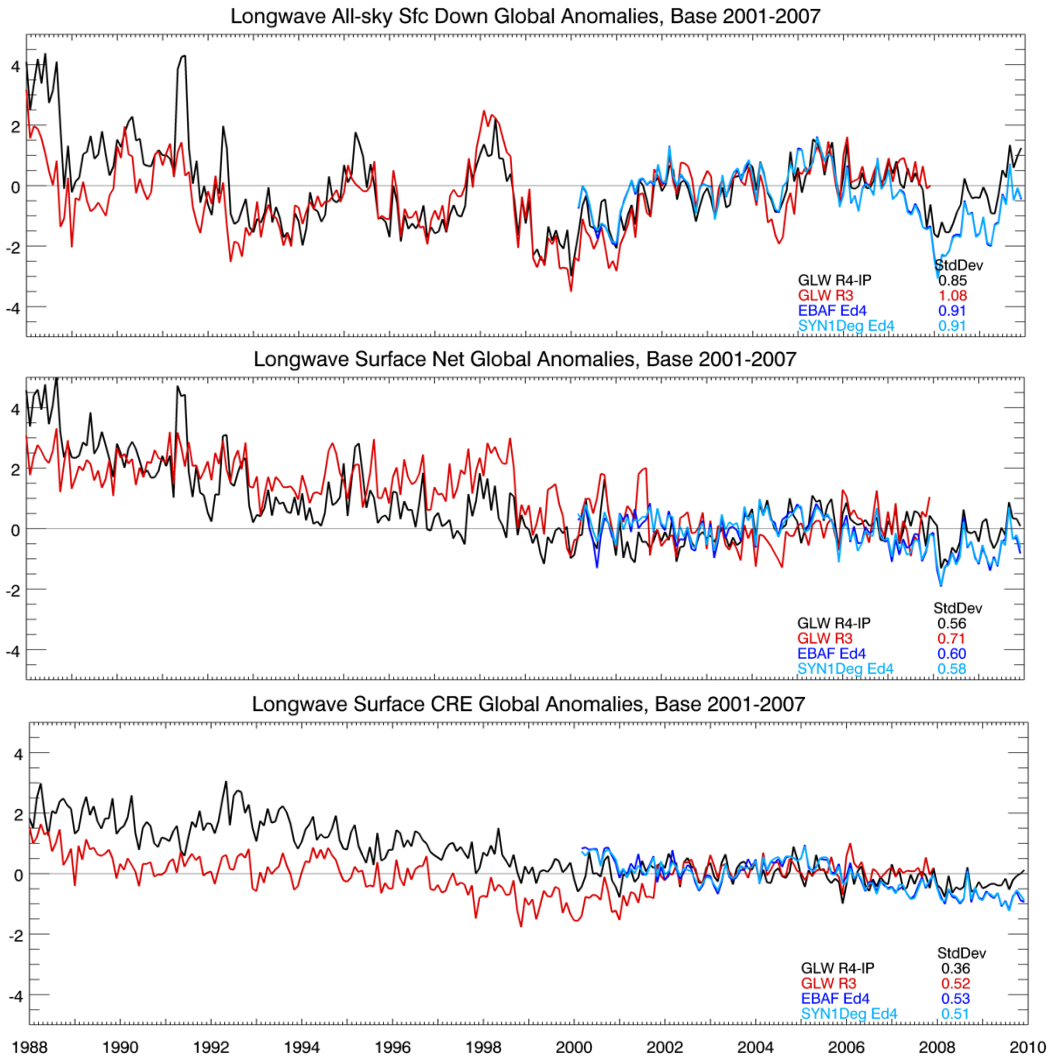

Figure 41. Surface longwave global monthly anomaly timeseries for the base years 2001-2007. Top panel is all-sky downward longwave, middle is net longwave, and bottom is cloud radiative effect. Rel4-IP is shown as the black line, Rel3.1 is in red, EBAF 4.1 is dark blue and SYN 1 Deg. Ed. 4A is light blue.

7.3.3 Total net comparisons and variability

As with the TOA total net flux, the surface total net flux exhibits characteristics of both longwave and shortwave fluxes. In some regions the differences between Rel4-IP and EBAF (Figure 42, left) are amplified by each, such as Northern Africa, where the large negative shortwave difference combines with the negative longwave difference. The positive ocean differences between Rel4-IP and ERA-5 (Figure 42, right) are larger than the difference with EBAF, but of similar spatial patterns. Additionally, since the ERA-5 difference also covers the time period in which there is no geostationary satellite coverage centered on 70°E longitude (see section 7.4.2), there are noticeable satellite ring differences. Figure 43 shows the long-term time series anomalies, the response to the eruption of Mt. Pinatubo is the prominent feature.

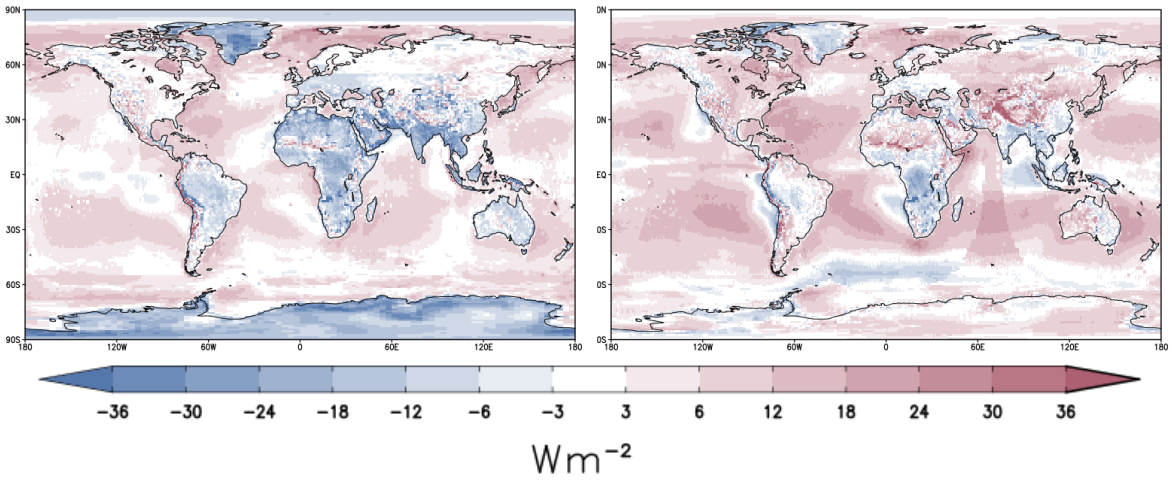

Figure 42. Surface total net (SW+LW) flux difference between Rel.4-IP and EBAF 4.1 (left) and Rel.4-IP and ERA5 (right) for the common over-lapping period of each.

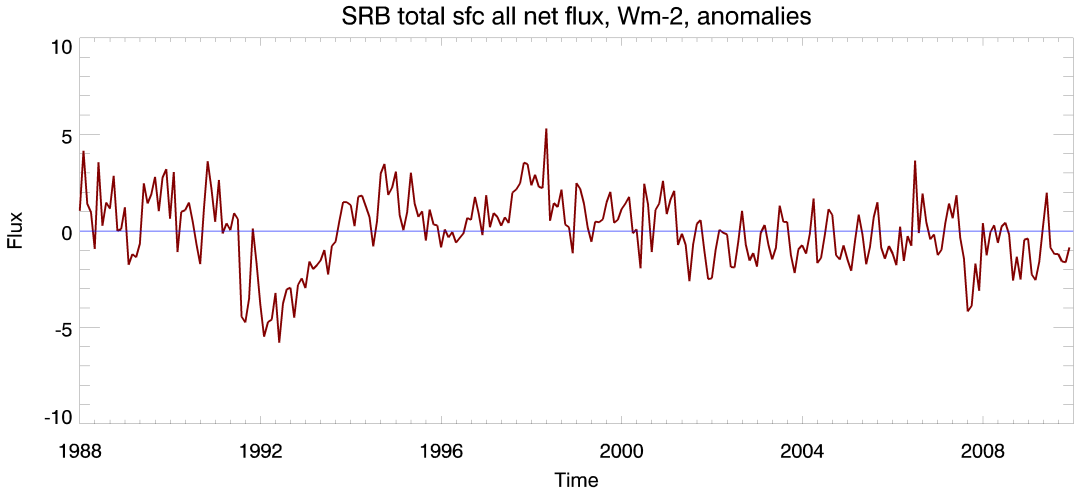

Figure 43. Surface total net (SW+LW) flux anomaly time series.

7.4 Known data issues

7.4.1 Incomplete GMS-2 coverage in 1984

From July through September 1984, the GMS-2 satellite in the ISCCP HXS dataset has 6-hourly coverage rather than the expected 3-hourly. The missing 3-hrly periods are covered by NOAA polar orbiter AVHRR overpasses, and by the filling algorithms where there is no coverage. The filling algorithms are meant to cover small and brief gaps rather than extended systematic gaps. The global fluxes in those months and the local fluxes over the GMS region of 90°E to 180° longitude, therefore, are less trustworthy and show greater variability.

From July through September 1984, the GMS-2 satellite in the ISCCP HXS dataset has 6-hourly coverage rather than the expected 3-hourly. The missing 3-hrly periods are covered by NOAA polar orbiter AVHRR overpasses, and by the filling algorithms where there is no coverage. The filling algorithms are meant to cover small and brief gaps rather than extended

systematic gaps. The global fluxes in those months and the local fluxes over the GMS region of 90°E to 180° longitude, therefore, are less trustworthy and show greater variability.

7.4.2 India gap

From 1983 through June 1998, there is a gap in geostationary coverage centered on 70°E longitude (Figure 44). In July 1998 Meteosat-5 was moved to fill this gap. Since that point, geostationary satellites cover the entirety of the globe from ~55°S to 55°N latitude. Prior to that point, the gap was only observed in the ISCCP dataset a few times per day by the polar orbiting NOAA satellites with onboard AVHRR instruments. In addition to the gap itself, the areas on the edges of the Meteosat and GMS satellite coverage areas rely on low satellite view angles and therefore generally show a bias towards higher cloud amounts. This is further manifested in SRB flux fields, as areas in the gap show higher shortwave fluxes at the surface than the nearby areas on the Meteosat and GMS edges. Filling the gap in July 1998 removes this artifact from the flux fields.

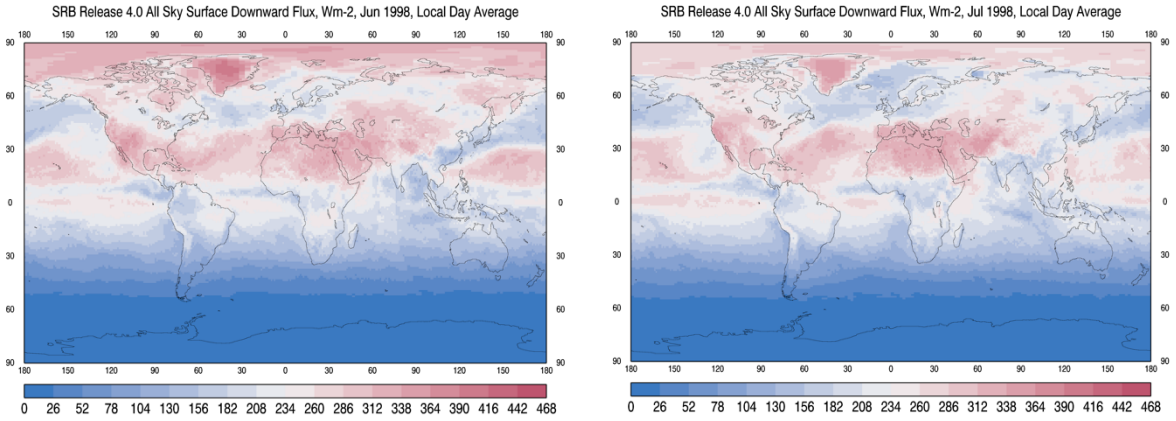

Figure 44. Shortwave surface downward flux for June 1998 (left), showing India gap in satellite coverage, and July 1998 (right), after gap is filled by Meteosat-5.

7.4.3 Loss of reference afternoon polar orbiter in 1994-5

ISCCP uses the AVHRR on the afternoon NOAA polar orbiter as a calibration standard for the other satellites in the dataset. Orbital drift necessitates the replacement of the afternoon orbiters every few years. The period from the retirement of NOAA-11 on September 30, 1994 and the activation of NOAA-14 on February 1, 1995 was a gap in coverage. An interpolation between the two is used as a calibration standard for the other satellites in this period. There are SRB flux anomalies which are likely the result of this gap.

7.4.4 Increased satellite coverage after 1998

The 1998 coverage of the India gap noted in section 7.4.2 immediately reduced the fraction of grid cells using filled values by several percentage points (Figure 45). This is the most significant but not only factor contributing to the less extensive satellite coverage of the first fifteen years of the ISCCP dataset. Temporal variability of the SRB fluxes (Figure 38, Figure 41) may be seen to be greater in this period.

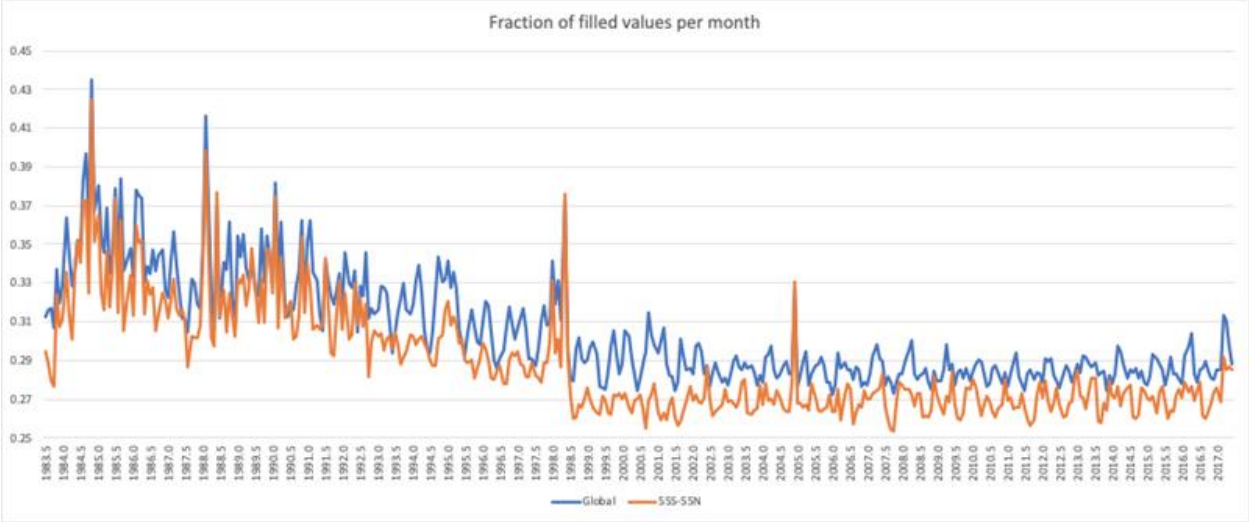

Figure 45. Fraction of grid cells relying on gap-filling algorithm. 55S-55N is mostly covered by the geostationary satellites. Note sudden drop in 1998 as the date Meteosat began covering the India gap.

7.4.5 A note on shortwave averaging

Fluxes are provided at 3-hourly, 3-hourly monthly, daily, and monthly timescales. The 3-hourly product is the basis for all other averages. Each 3-hourly flux is meant to provide the correct average integrated TOA incoming flux over that 3-hour period. The single solar zenith angle which instantaneously produces the period-average flux is chosen and all other fluxes are computed using this angle. If the period includes a sunset or sunrise, a zero TOA flux is assumed for integration purposes for all times the zenith angle is greater than 90°. No attempt at accounting for atmospheric refraction is performed.

The longer period averages are first computed by averaging the 3-hourly properties. An analytical daily average incoming TOA flux is computed. If the incoming TOA computed by the two methods differs, all the average fluxes are scaled by the ratio of the differences. In practice this is almost always a negligible correction on the order of 0.001 W m^{-2}. It will occasionally be a slightly greater correction in the polar twilight areas. The monthly averages are calculated from the daily averages with a similar correction made to the computed monthly average incoming TOA. The corrections are all within 0.1 W m^{-2}.

8 Conclusions

SRB Rel4-IP features full global coverage in shortwave and longwave for the period from 1988-2009. Shortwave extends full coverage back to July 1983 and forward to December 2017. Longwave land coverage goes back to July 1983 and longwave ocean coverage extends forward to December 2017. The length of the series allows full overlap with ERBE and with CERES products.

A key difference between Rel4-IP and Rel3 is the use of newly processed ISCCP H series data to replace the D series. This has increased cloud amount in the tropics while reducing it over polar regions. It has also changed the distribution of clouds with height, and the distribution of ice vs. liquid clouds. Shortwave and longwave calculations now include MACv1 aerosol, with explicit handling of asymmetry parameter and single scattering albedo. Other algorithmic improvements are described in sections 5 and 6.

Both shortwave and longwave products show good agreement with CERES products in terms of global averages and energy budget components. Shortwave TOA reflected flux is within 1 W m^{-2} (1.0%) of both CERES SYN1Deg and EBAF in the global annual mean. Longwave TOA OLR is within 1.4 W m^{-2} (0.6%). Shortwave surface downward flux is within 1.8 W m^{-2} (1.0%) and longwave surface downward flux is within 1.8 W m^{-2} (0.5%), but there are relatively large regional differences, however. Timeseries of global averages compared to CERES products show general good agreement, improved over Rel3.

Validation against land and ocean radiometric data show a slight longwave positive bias over both land (0.2 W m^{-2} Rel3, 0.8 W m^{-2} Rel4-IP, all numbers for monthly averages) and ocean (-1.6 W m^{-2} Rel3, 4.4 W m^{-2} Rel4-IP) with measures of variance similar to those found in Rel3 (land RMS 11.2 W m^{-2} Rel3, 15.9 W m^{-2} Rel4-IP, ocean 6.6 W m^{-2} Rel3, 7.9 W m^{-2} Rel4-IP). Shortwave bias has improved over land from strongly negative (-3.7 W m^{-2}, monthly average) in Rel3 to near zero (-0.8 W m^{-2}) in Rel4-IP. Shortwave variance measures are also uniformly improved over land (17.3 W m^{-2} RMS for Rel3, 14.2 W m^{-2} for Rel4-IP). Over ocean, shortwave biases improved from strongly positive (8.8 W m^{-2}) to near zero (0.6 W m^{-2}), again with improved variance (from an RMS of 15.1 to 12.6 W m^{-2}).

Longwave fluxes are strongly reliant on meteorological inputs. Limitations of NNHIRS data prevent its being used in lower atmospheric levels over ocean, where it is replaced with MERRA-2. Future improvements in SRB longwave fluxes will depend on improved meteorology datasets.

9 References

Bourlès, B., and Coauthors, 2008: THE PIRATA PROGRAM: History, Accomplishments, and Future Directions. *Bull. Amer. Meteor. Soc.*, **89**, 1111–1126, https://doi.org/10.1175/2008BAMS2462.1.

Briegleb, B. P., P. Minnis, V. Ramanathan, and E. Harrison, 1986: Comparison of Regional Clear-Sky Albedos Inferred from Satellite Observations and Model Computations. *J. Climate Appl. Meteor.*, **25**, 214–226, https://doi.org/10.1175/1520-0450(1986)025<0214:CORCSA>2.0.CO;2.

Clayson, C. A., J. Brown, and NOAA CDR Program, 2016a: NOAA Climate Data Record (CDR) of Ocean Near Surface Atmospheric Properties, Version 2. https://doi.org/10.7289/V55T3HH0(2017-2020).

——, ——, and ——, 2016b: NOAA Climate Data Record (CDR) of Sea Surface Temperature - WHOI, Version 2. https://doi.org/10.7289/V5FB510W(2017-2020).

Coccia, G., A. L. Siemann, M. Pan, and E. F. Wood, 2015: Creating consistent datasets by combining remotely-sensed data and land surface model estimates through Bayesian uncertainty post-processing: The case of Land Surface Temperature from HIRS. *Remote Sensing of Environment*, **170**, 290–305, https://doi.org/10.1016/j.rse.2015.09.010.

Collins, W. D., P. J. Rasch, B. E. Eaton, B. V. Khattatov, J.-F. Lamarque, and C. S. Zender, 2001: Simulating aerosols using a chemical transport model with assimilation of satellite aerosol retrievals: Methodology for INDOEX. *J. Geophys. Res.*, **106**, 7313–7336, https://doi.org/10.1029/2000JD900507.

Froidevaux, L., and Coauthors, 2015: Global OZone Chemistry And Related trace gas Data records for the Stratosphere (GOZCARDS): methodology and sample results with a focus on HCl, H_2O, and O_3. *Atmospheric Chemistry and Physics*, **15**, 10471–10507, https://doi.org/10.5194/acp-15-10471-2015.

Fu, Q., and K. N. Liou, 1992: On the Correlated k-Distribution Method for Radiative Transfer in Nonhomogenecous Atmospheres. *Journal of the Atmospheric Sciences*, **49**, 2139–2156.

——, K. N. Liou, M. C. Cribb, T. P. Charlock, and A. Grossman, 1997: Multiple Scattering Parameterization in Thermal Infrared Radiative Transfer. *Journal of the Atmospheric Sciences*, **54**, 2799–2812.

——, P. Yang, and W. B. Sun, 1998: An Accurate Parameterization of the Infrared Radiative Properties of Cirrus Clouds for Climate Models. *Journal of Climate*, **11**, 2223–2237.

Gelaro, R., and Coauthors, 2017: The Modern-Era Retrospective Analysis for Research and Applications, Version 2 (MERRA-2). *J. Climate*, **30**, 5419–5454, https://doi.org/10.1175/JCLI-D-16-0758.1.

Global Modeling and Assimilation Office (GMAO), 2015a: MERRA-2 tavgM_2d_rad_Nx: 2d,Monthly mean,Time-Averaged,Single-Level,Assimilation,Radiation Diagnostics V5.12.4, Greenbelt, MD, USA, Goddard Earth Sciences Data and Information Services Center (GES DISC), Accessed: Nov. 2020, https://doi.org/10.5067/OU3HJDS973O0.

——, 2015b: MERRA-2 tavgM_2d_slv_Nx: 2d, Monthly mean,Time-Averaged,Single-Level,Assimilation,Radiation Diagnostics V5.12.4, Greenbelt, MD, USA, Goddard Earth Sciences Data and Information Services Center (GES DISC), Accessed: July 2019, https://doi.org/10.5067/AP1B0BA5PD2K.

——, 2015c: MERRA-2 tavg1_2d_slv_Nx: 2d,1-Hourly,Time-Averaged,Single-Level,Assimilation,Single-Level Diagnostics V5.12.4, Greenbelt, MD, USA, Goddard Earth Sciences Data and Information Services Center (GES DISC), Accessed: July 2019, https://doi.org/10.5067/VJAFPLI1CSIV.

——, 2015d: MERRA-2 inst3_3d_asm_Np: 3d,3-Hourly,Instantaneous,Pressure-Level,Assimilation,Assimilated Meteorological Fields V5.12.4, Greenbelt, MD, USA, Goddard Earth Sciences Data and Information Services Center (GES DISC), Accessed: July 2019, https://doi.org/10.5067/QBZ6MG944HW0.

Huang, X., X. Chen, D. K. Zhou, and X. Liu, 2016: An Observationally Based Global Band-by-Band Surface Emissivity Dataset for Climate and Weather Simulations. *Journal of the Atmospheric Sciences*, **73**, 3541–3555, https://doi.org/10.1175/JAS-D-15-0355.1.

Jin, Z., K. Stamnes, W. F. Weeks, and S.-C. Tsay, 1994: The effect of sea ice on the solar energy budget in the atmosphere-sea ice-ocean system: A model study. *Journal of Geophysical Research: Oceans*, **99**, 25281–25294, https://doi.org/10.1029/94JC02426.

——, T. P. Charlock, W. L. Smith, and K. Rutledge, 2004: A parameterization of ocean surface albedo: OCEAN SURFACE ALBEDO. *Geophys. Res. Lett.*, **31**, https://doi.org/10.1029/2004GL021180.

Kinne, S., and Coauthors, 2013: MAC-v1: A new global aerosol climatology for climate studies: MAC-v1 for Climate Studies. *J. Adv. Model. Earth Syst.*, **5**, 704–740, https://doi.org/10.1002/jame.20035.

Kopp, G., and J. L. Lean, 2011: A new, lower value of total solar irradiance: Evidence and climate significance. *Geophysical Research Letters*, **38**, https://doi.org/10.1029/2010GL045777.

Kummerow, C., and Coauthors, 2019: The GDAP Integrated Product. *GEWEX News*, **29**.

Loeb, N. G., D. R. Doelling, H. Wang, W. Su, C. Nguyen, J. G. Corbett, L. Liang, C. Mitrescu, F. G. Rose, and S. Kato. "Clouds and the Earth's Radiant Energy System (CERES) Energy Balanced and Filled (EBAF) Top-of-Atmosphere (TOA) Edition-4.0 Data Product." *Journal of Climate* 31, no. 2 (January 15, 2018): 895–918. https://doi.org/10.1175/JCLI-D-17-0208.1.

Matthews, E., 1985: *Atlas of archived vegetation and land use and seasonal albedo data sets*. NASA.

McClatchey, R. A., R. W. Fenn, E. A. Selby, F. E. Volz, and J. S. Garing, *Optical properties of the atmosphere*.

McPhaden, M. J., and Coauthors, 1998: The Tropical Ocean-Global Atmosphere observing system: A decade of progress. *J. Geophys. Res.*, **103**, 14169–14240, https://doi.org/10.1029/97JC02906.

McPhaden, M. J., and Coauthors, 2009: RAMA: The Research Moored Array for African–Asian–Australian Monsoon Analysis and Prediction [*]. *Bull. Amer. Meteor. Soc.*, **90**, 459–480, https://doi.org/10.1175/2008BAMS2608.1.

Mears, C. A., and F. J. Wentz, 2009: Construction of the RSS V3.2 Lower-Tropospheric Temperature Dataset from the MSU and AMSU Microwave Sounders. *Journal of Atmospheric and Oceanic Technology*, **26**, 1493–1509, https://doi.org/10.1175/2009JTECHA1237.1.

——, and ——, 2017: A Satellite-Derived Lower-Tropospheric Atmospheric Temperature Dataset Using an Optimized Adjustment for Diurnal Effects. *Journal of Climate*, **30**, 7695–7718, https://doi.org/10.1175/JCLI-D-16-0768.1.

Ohmura, A., and Coauthors, 1998: Baseline Surface Radiation Network (BSRN/WCRP): New Precision Radiometry for Climate Research. *Bulletin of the American Meteorological Society*, **79**, 2115–2136, https://doi.org/10.1175/1520-0477(1998)079<2115:BSRNBW>2.0.CO;2.

Pinker, R. T., and I. Laszlo, 1992: Modeling Surface Solar Irradiance for Satellite Applications on a Global Scale. *J. Appl. Meteor.*, **31**, 194–211, https://doi.org/10.1175/1520-0450(1992)031<0194:MSSIFS>2.0.CO;2.

Rose, F. G., D. A. Rutan, T. Charlock, G. L. Smith, and S. Kato, 2013: An Algorithm for the Constraining of Radiative Transfer Calculations to CERES-Observed Broadband Top-of-Atmosphere Irradiance. *J. Atmos. Oceanic Technol.*, **30**, 1091–1106, https://doi.org/10.1175/JTECH-D-12-00058.1.

Rossow, W., V. Golea, A. Walker, K. Knapp, A. Young, B. Hankins, and A. Inamdar, 2017: International Satellite Cloud Climatology Project (ISCCP) Climate Data Record, H-Series. https://doi.org/10.7289/V5QZ281S.

Rossow, W. B., 2017: *Climate Data Record Program (CDRP): Climate Algorithm Theoretical Basis Document (C-ATBD) International Satellite Cloud Climatology Project (ISCCP) H-Series*.

Rossow, W. B., A. Walker, D. E. Beuschel, and M. D. Roiter, 1996: *International Satellite Cloud Climatology Project (ISCCP) Documentation of New Cloud Datasets*. WMO/TD-737, 115pp.

Rutan, D. A., S. Kato, D. R. Doelling, F. G. Rose, L. T. Nguyen, T. E. Caldwell, and N. G. Loeb, 2015: CERES Synoptic Product: Methodology and Validation of Surface Radiant Flux. *Journal of Atmospheric and Oceanic Technology*, **32**, 1121–1143, https://doi.org/10.1175/JTECH-D-14-00165.1.

Schröder, M., and Coauthors, 2018: The GEWEX Water Vapor Assessment archive of water vapour products from satellite observations and reanalyses. *Earth Syst. Sci. Data*, **10**, 1093–1117, https://doi.org/10.5194/essd-10-1093-2018.

——, and Coauthors, 2019: The GEWEX Water Vapor Assessment: Overview and Introduction to Results and Recommendations. *Remote Sensing*, **11**, 251, https://doi.org/10.3390/rs11030251.

Shi, L., J. Matthews, S. Ho, Q. Yang, and J. Bates, 2016: Algorithm Development of Temperature and Humidity Profile Retrievals for Long-Term HIRS Observations. *Remote Sensing*, **8**, 280, https://doi.org/10.3390/rs8040280.

Stackhouse Jr, P. W., S. K. Gupta, S. J. Cox, T. Zhang, and J. C. Mikovitz, 2011: The NASA/GEWEX Surface Radiation Budget Release 3.0: 24.5-Year Dataset. *GEWEX News*, **21**, 10–12.

Suarez, M., S. Bloom, A. daSilva, D. Dee, M. Bosilovich, and et al., 2005: *Documentation and Validation of the Goddard Earth Observing System (GEOS) Data Assimilation System, Version 4*., **26,** 181pp., NASA/TM-2005-104606.

Suttles, J. T., and G. Ohring, 1986: *Surface radiation budget for climate applications*. NASA Rep, **1169**, 136pp.

Werdell, P. J., and S. W. Bailey, 2005: An improved in-situ bio-optical data set for ocean color algorithm development and satellite data product validation. *Remote Sensing of Environment*, **98**, 122–140, https://doi.org/10.1016/j.rse.2005.07.001.

Whitlock, C. H., and Coauthors, 1995: First Global WCRP Shortwave Surface Radiation Budget Dataset. *Bull. Amer. Meteor. Soc.*, **76**, 905–922, https://doi.org/10.1175/1520-0477(1995)076<0905:FGWSSR>2.0.CO;2.

Wild, M., and Coauthors, 2015: The energy balance over land and oceans: an assessment based on direct observations and CMIP5 climate models. *Clim Dyn*, **44**, 3393–3429, https://doi.org/10.1007/s00382-014-2430-z.

Wiscombe, W. J., and S. G. Warren, 1980: A Model for the Spectral Albedo of Snow. I: Pure Snow. *J. Atmos. Sci.*, **37**, 2712–2733, https://doi.org/10.1175/1520-0469(1980)037<2712:AMFTSA>2.0.CO;2.

Young, A. H., K. R. Knapp, A. Inamdar, W. Hankins, and W. B. Rossow, 2018: The International Satellite Cloud Climatology Project H-Series climate data record product. *Earth Syst. Sci. Data*, **10**, 583–593, https://doi.org/10.5194/essd-10-583-2018.

Zhang, T., P. W. Stackhouse, S. K. Gupta, S. J. Cox, J. Colleen Mikovitz, and L. M. Hinkelman, 2013: The validation of the GEWEX SRB surface shortwave flux data products using

BSRN measurements: A systematic quality control, production and application approach. *Journal of Quantitative Spectroscopy and Radiative Transfer*, **122**, 127–140, https://doi.org/10.1016/j.jqsrt.2012.10.004.

——, ——, ——, ——, and J. C. Mikovitz, 2015: The validation of the GEWEX SRB surface longwave flux data products using BSRN measurements. *Journal of Quantitative Spectroscopy and Radiative Transfer*, **150**, 134–147, https://doi.org/10.1016/j.jqsrt.2014.07.013.

——, ——, ——, ——, and ——, 2017: A generalized formulation for downscaling data based on Fourier Transform and inversion: Mathematical rationale and application to the Max-Planck-Institute aerosol climatology data. *Journal of Quantitative Spectroscopy and Radiative Transfer*, **188**, 176–180, https://doi.org/10.1016/j.jqsrt.2016.08.019.

——, ——, S. J. Cox, and J. C. Mikovitz, 2020: The uncertainty of the BSRN monthly mean Global 1 and Global 2 fluxes due to missing hourly means with and without quality-control and an examination through validation of the NASA GEWEX SRB datasets. *Journal of Quantitative Spectroscopy and Radiative Transfer*, **255**, 107272, https://doi.org/10.1016/j.jqsrt.2020.107272.

Appendix A. Abbreviations and Acronyms

ATBD	Algorithm Theoretical Basis Document
AVHRR	Advanced Very-High-Resolution Radiometer
BSRN	Baseline Surface Radiation Network
CERES	Clouds and the Earth's Radiant Energy System
DLF	Downwelling Longwave Flux
EBAF	Energy Balance and Filled
ECMWF	European Centre for Medium-Range Weather Forecasts
ERA-5	ECMWF ReAnalysis v5
ERBE	Earth Radiation Budget Experiment
GDAP	GEWEX Data and Assessments Panel
GEWEX	Global Energy and Water-cycle Exchanges
GMAO	Global Modeling and Assimilation Office
GMS	Geostationary Meteorological Satellite
GSW	GEWEX Shortwave
HIRS	High-Resolution Infra-Red Sounder
IR	Infrared
ISCCP	International Satellite Cloud Climatology Project
LaRC	Langley Research Center
LW	Longwave
MAC	Max-Planck Aerosol Climatology
MATCH	Model of Atmospheric Transport and Chemistry
MERRA-2	Modern Era Retrospective Analysis for Research and Applications
NASA	National Aeronautics and Space Administration
NIR	Near-IR
NNHIRS	Neural Network High-Resolution Infra-Red Sounder
OLR	Outgoing Longwave Radiation
OMI	Ozone Monitoring Instrument
NOAA	National Oceanic and Atmospheric Administration
PMEL	Pacific Marine Environmental Laboratory
Rel4-IP	Release 4-Integrated Product
RMS	Root Mean Square
RSS	Remote Sensing Systems
Sfc	Surface
SRB	Surface Radiation Budget
SMOBA	Stratosphere Monitoring Ozone Blended Analysis
SW	Shortwave
SYN1Deg	(CERES) Synoptic 1-Degree
TOA	Top-of-atmosphere
TOMS	Total Ozone Mapping Spectrometer
TOVS	TIROS Operation Vertical Sounder
WCRP	World Climate Research Programme

Appendix B. GEWEX SRB Nested Grid

Although GEWEX SRB R4-IP data products are provided at the 1° x 1° latitude/longitude grid resolution, the satellite data products and radiative transfer algorithms are applied to a quasi-equal area grid, referred to as the "nested" grid. This nested grid better maintains consistency of sampling per grid box as the longitudinal extent of 1° x 1° grid boxes in terms of length scale (i.e., km) shrinks towards the poles. The fluxes are generated on a nested grid, which contains 44016 grid cells. The grid has a resolution of 1° latitude globally, and longitudinal resolution ranging from 1° in the tropics and subtropics to 120 degrees at the poles. The first cell is Latitude 89° -90° degrees South, Longitude 0-120 degrees East. The cells start at the Greenwich meridian and proceed east around the globe, then shift one degree to the north. The number of cells per latitude band starting at the South Pole are:

Latitude Band	# of Grid Cells per latitudinal zone	Longitudinal Extent
89° - 90° N/S	3	120°
80° - 89° N/S	45	8°
70° - 80° N/S	90	4°
45° - 70° N/S	180	2°
45° S - 45° N	360	1°

All data products are remapped to a true equal angle 1° x 1° grid system for delivery to users.